PHYSICAL REVIEW D **85,** 114508 (2012)

Calculation of the heavy-hadron axial couplings g_1, g_2, and g_3 using lattice QCD

William Detmold,[1,2,*] C.-J. David Lin,[3,4,†] and Stefan Meinel[1,‡]

[1]*Department of Physics, College of William and Mary, Williamsburg, Virginia 23187, USA*
[2]*Jefferson Laboratory, 12000 Jefferson Avenue, Newport News, Virginia 23606, USA*
[3]*Institute of Physics, National Chiao-Tung University, Hsinchu 300, Taiwan*
[4]*Physics Division, National Centre for Theoretical Sciences, Hsinchu 300, Taiwan*

(Received 19 March 2012; published 18 June 2012)

In a recent letter [Phys. Rev. Lett. **108**, 172003 (2012)] we have reported on a lattice QCD calculation of the heavy-hadron axial couplings g_1, g_2, and g_3. These quantities are low-energy constants of heavy-hadron chiral perturbation theory (HHχPT) and are related to the $B^*B\pi$, $\Sigma_b^*\Sigma_b\pi$, and $\Sigma_b^{(*)}\Lambda_b\pi$ couplings. In the following, we discuss important details of the calculation and give further results. To determine the axial couplings, we explicitly match the matrix elements of the axial current in QCD with the corresponding matrix elements in HHχPT. We construct the ratios of correlation functions used to calculate the matrix elements in lattice QCD, and study the contributions from excited states. We present the complete numerical results and discuss the data analysis in depth. In particular, we demonstrate the convergence of $SU(4|2)$ HHχPT for the axial-current matrix elements at pion masses up to about 400 MeV and show the impact of the nonanalytic loop contributions. Finally, we present additional predictions for strong and radiative decay widths of charm and bottom baryons.

DOI: 10.1103/PhysRevD.85.114508 PACS numbers: 12.38.Gc, 12.39.Fe, 12.39.Hg, 14.20.Mr

I. INTRODUCTION

Two important symmetries which allow many predictions in nonperturbative QCD are chiral symmetry [1] and heavy-quark symmetry [2]. Both symmetries are a consequence of the large separation of scales in the quark masses, relative to the intrinsic scale of QCD. In chiral perturbation theory, an expansion is performed around the limit where the light-quark masses vanish, and the dynamics is determined by derivatively coupled pions, associated with the spontaneous breaking of chiral symmetry. In heavy-quark effective theory, an expansion is performed around the static limit, where a quark mass is infinitely heavy. In that limit, the heavy quark acts as a pointlike color source with a fixed velocity, and the spin of the heavy quark decouples. Corrections to the static limit are suppressed by powers of $\Lambda_{\rm QCD}/m_Q$, where m_Q is the heavy-quark mass. Because $\Lambda_{\rm QCD}/m_b$ is particularly small, the static limit is a good approximation to describe the dynamics of hadrons containing a bottom quark. For charmed hadrons, the static limit is still a reasonable first approximation.

At the hadronic level, the combination of chiral symmetry and heavy-quark symmetry into a single effective theory leads to a framework known as heavy-hadron chiral perturbation theory (HHχPT), which describes the interactions of heavy-light hadrons with pions and kaons [3–8]. At leading order, the HHχPT Lagrangian contains three axial couplings g_1, g_2 and g_3. The coupling g_1 determines the strength of the interaction between heavy-light mesons and pions, while g_2 and g_3 similarly determine the interaction of heavy-light baryons with pions.

In the meson sector, the strong decay $B^* \to B\pi$ is kinematically forbidden. However, virtual pion loops contribute to much of the physics of B mesons, and the coupling g_1 appears in calculations of important observables such as B meson masses, decay constants, bag parameters and form factors within chiral perturbation theory [9–11]. Precise knowledge of these hadronic observables is needed for flavor physics, both within and beyond the standard model. In this context, chiral perturbation theory is needed, in particular, to describe the quark-mass dependence of lattice QCD results for such observables. Most current lattice QCD calculations are performed at unphysically large values of the up- and down-quark masses to reduce the amount of computer time needed. The results from a range of quark masses must then be extrapolated to the physical values of the light-quark masses. Chiral perturbation theory predicts the functional form needed for this extrapolation, but the uncertainty in the final result is influenced significantly by the uncertainty in the value of the axial coupling g_1 [12].

While most of heavy-flavor physics has traditionally focused on the B mesons, measurements at the LHC and super-B factories will extend the knowledge of flavor physics in the bottom-baryon sector, which provides complementary constraints on new physics models because of the different spin of the baryons. Therefore, lattice QCD calculations of bottom-baryon observables such as form factors are needed, and as in the meson sector, chiral extrapolations of the data need to be performed. For baryons, the accuracy of such extrapolations can be improved

*wdetmold@jlab.org
†dlin@mail.nctu.edu.tw
‡smeinel@wm.edu

dramatically if the values of the couplings g_2 and g_3 are known. The coupling g_3 is related to the strong decays $\Sigma_b^{(*)} \to \Lambda_b \pi$, which are kinematically allowed. The widths of these decays have recently been measured at Fermilab [13], but the experimental uncertainty is still large.

The axial couplings g_1, g_2, and g_3 are calculable from the underlying theory, QCD. The only reliable approach for these nonperturbative observables is lattice QCD. While there are no previous lattice calculations of g_2 and g_3, a number of groups have performed lattice computations of the coupling g_1, both in the quenched approximation (i.e., neglecting the vacuum-polarization effects of light quarks) [14–16] and with $n_f = 2$ dynamical flavors [17–19]. In these lattice calculations, one computes matrix elements of the axial current, and relates these matrix elements to the coupling g_1. To fit the data and extract g_1, theoretical knowledge of the light-quark-mass dependence of the axial-current matrix elements is required. The previous lattice calculations used fits that were linear or quadratic in the pion mass, or including logarithms, but the correct chiral perturbation theory predictions were not known.

We have recently derived the expressions for the axial-current matrix elements at next-to-leading order in partially quenched heavy-hadron chiral perturbation theory, both for the mesons and the baryons [20]. We have then performed the first complete lattice QCD calculation of the three axial couplings g_1, g_2, g_3, controlling all systematic uncertainties [21]. In the following, we discuss important details of the analysis that were omitted for brevity in Ref. [21], and present some additional results.

Our calculation includes $n_f = 2 + 1$ flavors of dynamical light quarks, and makes use of data at six different values of the quark masses corresponding to (valence) pion masses as low as 227 MeV. Two different lattice spacings of $a = 0.112$ fm and $a = 0.085$ fm are used to perform a continuum extrapolation. The spatial volume is $(2.7\ \text{fm})^3$, large enough so that finite-size effects are very small and can be removed by using finite-volume heavy-hadron chiral perturbation theory in the p regime. Because the axial couplings g_1, g_2, g_3 are defined in the static limit, we use the static lattice action of Ref. [22], modified using smeared gauge links to reduce noise [23], for the heavy quark. We implement the light quarks with a domain-wall action [24–26]. This is a five-dimensional formulation that realizes a lattice chiral symmetry for the four-dimensional theory, which becomes exact, even at finite lattice spacing, when the extent of the auxiliary fifth dimension is taken to infinity. As a result, the renormalization of operators is simplified and discretization errors are small. Our calculations make use of gauge field ensembles generated by the RBC and UKQCD collaborations [27].

This paper is organized as follows: We begin with an introduction to HHχPT in Sec. II A. We derive the matrix elements of the axial Noether current at leading order in HHχPT using canonical quantization in Sec. II B. The ratios of correlation functions used to calculate the corresponding matrix elements in lattice QCD are constructed in Sec. II C, where we also show their spectral decomposition. The details of the lattice actions and parameters are given in Sec. III. We present the numerical results for the ratios of correlation functions in Sec. IV A, and explain our method for extracting the ground-state contributions to the matrix elements in Sec. IV B. In Sec. IV C, we then describe the chiral fits using $SU(4|2)$ HHχPT, including the effects of finite volume and nonzero lattice spacing. We compare our lattice QCD results for the axial couplings to various estimates reported in the literature in Sec. V. The calculations of heavy-baryon decay widths are presented in Sec. VI, and we conclude in Sec. VII. Appendix A contains further plots of numerical data, and Appendix B contains a comparison of our ratio method with an alternative approach (the summation method).

II. AXIAL COUPLINGS FROM RATIOS OF CORRELATION FUNCTIONS

A. Heavy-hadron chiral perturbation theory

For hadrons containing a heavy quark (or antiquark), in the static limit $m_Q \to \infty$, the spin of the light degrees of freedom, s_l, becomes a conserved quantum number. The lowest-lying static-light mesons have $s_l = 1/2$, and are therefore grouped into pseudoscalar mesons, described by a field P^i, and vector mesons, described by a field P^{*i}_μ. We work with heavy-light mesons containing a light quark of flavor $i = u, d$ and a heavy antiquark. The vector meson field satisfies $v^\mu P^{*i}_\mu = 0$, where v is the four-velocity; this is a parameter of the effective theory, subject to the constraint $v^2 = 1$. Because of heavy-quark spin symmetry, the pseudoscalar and vector mesons are degenerate. To make the heavy-quark symmetry manifest, the pseudoscalar and vector meson fields can be combined into a single field H, which is 4×4-matrix-valued and given by [3,9]

$$H^i = [-P^i \gamma_5 + P^{*i}_\mu \gamma^\mu] \frac{1 - \not{v}}{2}. \tag{1}$$

This field satisfies the constraint $H^i \frac{1-\not{v}}{2} = H^i$. Next, we consider static-light baryons containing two light quarks of flavors i and j and a heavy quark. We include both the states with $s_l = 0$ and $s_l = 1$. The states with $s_l = 1$ form two multiplets with $J = 1/2$ and $J = 3/2$, and are described by a Dirac spinor field B^{ij} and a Rarita-Schwinger spinor field B^{*ij}_μ. These $s_l = 1$ fields are symmetric in flavor: $B^{ij} = B^{ji}$ and $B^{*ij}_\mu = B^{*ji}_\mu$. For two quark flavors one has (using the notation for bottom baryons)

$$B = \begin{pmatrix} \Sigma_b^+ & \frac{1}{\sqrt{2}} \Sigma_b^0 \\ \frac{1}{\sqrt{2}} \Sigma_b^0 & \Sigma_b^- \end{pmatrix}, \tag{2}$$

and similarly for B^*_μ. Again, because of heavy-quark spin symmetry, the $J = 1/2$ and $J = 3/2$ baryons with $s_l = 1$

are degenerate, and the corresponding fields can be combined into a single field [7,28],

$$S_\mu^{ij} = S_\mu^{ji} = \sqrt{\frac{1}{3}}(\gamma_\mu + v_\mu)\gamma_5 B^{ij} + B_\mu^{*ij}, \tag{3}$$

satisfying $v^\mu S_\mu^{ij} = 0$ and $\frac{1+\not{v}}{2} S_\mu^{ij} = S_\mu^{ij}$. The $s_l = 0$ baryons have $J = 1/2$ and can be described by a Dirac spinor field T^{ij}, which is antisymmetric in i and j and satisfies the constraint $\frac{1+\not{v}}{2} T^{ij} = T^{ij}$. For two quark flavors, one has

$$T = \frac{1}{\sqrt{2}} \begin{pmatrix} 0 & \Lambda_b \\ -\Lambda_b & 0 \end{pmatrix}. \tag{4}$$

In $SU(2)$ chiral perturbation theory, the pions are described by an $SU(2)$-valued field $\Sigma = \exp(2i\Phi/f)$, which transforms under global $SU(2)_L \times SU(2)_R$ transformations as

$$\Sigma \to L\Sigma R^\dagger. \tag{5}$$

For the purposes of heavy-hadron chiral perturbation theory, it is convenient to also introduce the field $\xi = \exp(i\Phi/f)$, so that $\Sigma = \xi^2$. The field ξ transforms as

$$\xi \to L\xi U^\dagger = U\xi R^\dagger, \tag{6}$$

where the transformation matrix $U(x)$ is a function of L, R and $\Phi(x)$, implicitly defined through the above equations. Under the vector subgroup $L = R = V$, the field ξ transforms as $\xi \to V\xi V^\dagger$. Therefore, the natural transformation laws for the heavy-hadron fields also involve the matrix U:

$$\begin{aligned} H^i &\to U^i{}_j H^j, \qquad S_\mu^{ij} \to U^i{}_k U^j{}_l S_\mu^{kl}, \\ T^{ij} &\to U^i{}_k U^j{}_l T^{kl}. \end{aligned} \tag{7}$$

The leading-order heavy-hadron chiral perturbation theory Lagrangian is then given by [5–8]

$$\begin{aligned} \mathcal{L} = {} & \frac{f^2}{8}(\partial^\mu \Sigma^\dagger)_{ij}\partial_\mu \Sigma^{ji} - i\,\mathrm{tr}_D[\bar{H}_i v\cdot\mathcal{D}H^i] - i\bar{S}_{ij}^\mu v\cdot\mathcal{D}S_\mu^{ij} + i\bar{T}_{ij} v\cdot\mathcal{D}T^{ij} + \Delta\bar{S}_{ij}^\mu S_\mu^{ij} + g_1\,\mathrm{tr}_D[\bar{H}_i(\mathcal{A}^\mu)^i{}_j\gamma_\mu\gamma_5 H^j] \\ & - ig_2\epsilon_{\mu\nu\sigma\lambda}\bar{S}_{ki}^\mu v^\nu(\mathcal{A}^\sigma)^i{}_j(S^\lambda)^{jk} + \sqrt{2}g_3[\bar{S}_{ki}^\mu(\mathcal{A}_\mu)^i{}_j T^{jk} + \bar{T}_{ki}(\mathcal{A}^\mu)^i{}_j S_\mu^{jk}] + (m_q \text{ terms}) + (1/m_Q \text{ terms}), \end{aligned} \tag{8}$$

where tr_D denotes the trace in Dirac space, and the covariant derivatives are defined as

$$\begin{aligned} \mathcal{D}^\mu H^i &= \partial^\mu H^i + (\mathcal{V}^\mu)^i{}_j H^j, \\ \mathcal{D}^\mu S_\nu^{ij} &= \partial^\mu S_\nu^{ij} + (\mathcal{V}^\mu)^i{}_k S_\nu^{kj} + (\mathcal{V}^\mu)^j{}_k S_\nu^{ik}, \\ \mathcal{D}^\mu T^{ij} &= \partial^\mu T^{ij} + (\mathcal{V}^\mu)^i{}_k T^{kj} + (\mathcal{V}^\mu)^j{}_k T^{ik}, \end{aligned} \tag{9}$$

with the vector and axial-vector fields

$$\begin{aligned} \mathcal{V}^\mu &= \frac{1}{2}(\xi^\dagger\partial^\mu\xi + \xi\partial^\mu\xi^\dagger), \\ \mathcal{A}^\mu &= \frac{i}{2}(\xi^\dagger\partial^\mu\xi - \xi\partial^\mu\xi^\dagger). \end{aligned} \tag{10}$$

The H and T fields are rescaled such that their masses do not appear in the Lagrangian. The quantity Δ is the mass difference between the S and T baryons. This mass difference does not vanish in the chiral limit nor in the heavy-quark limit. From experiment, one has $\Delta \approx 200$ MeV [13,29].

Our definitions of the axial couplings g_1, g_2, and g_3 in Eq. (8) are related to the definitions of Yan *et al.* [5] and Cho [7] as follows [30]:

$$\begin{aligned} g_1 = g_1^{(\mathrm{Cho})} = g^{(\mathrm{Yan})}, \qquad g_2 = -g_2^{(\mathrm{Cho})} = \tfrac{3}{2} g_1^{(\mathrm{Yan})}, \\ g_3 = g_3^{(\mathrm{Cho})} = -\sqrt{3} g_2^{(\mathrm{Yan})}. \end{aligned} \tag{11}$$

We introduced the minus sign on g_2 relative to the definition by Cho, so that in our conventions all three couplings are positive.

The Lagrangian (8) has the same form for both $SU(2)$ and $SU(3)$ chiral perturbation theory, the only difference being that the flavor indices run from 1 to 2 and 1 to 3, respectively. The theory can be generalized to the partially quenched $SU(4|2)$ or $SU(6|3)$ cases, where the valence and sea quarks can have different masses; for more details see [20] and the references therein.

As can be seen by expanding the field $\xi = \exp(i\Phi/f)$ in Eq. (8) in terms of the pion field Φ, at lowest order the term with the axial coupling g_1 leads to an H-H-Φ vertex, the term with the coupling g_2 leads to an S-S-Φ vertex, and finally the term with the coupling g_3 leads to an S-T-Φ vertex.

B. Axial-current matrix elements in heavy-hadron chiral perturbation theory

The simplest quantities that depend on the axial couplings are the matrix elements of the axial currents between single-hadron states (an alternative approach to determine the axial couplings based on static hadron-hadron potentials is discussed in Ref. [31]). To extract g_1, g_2, and g_3, we will calculate the matrix elements of the axial current in both χPT and (lattice) QCD, and match the two with each other:

$$\langle X|A_\mu^{(\mathrm{QCD})}|Y\rangle_{\mathrm{QCD}} = \langle X|A_\mu^{(\chi\mathrm{PT})}|Y\rangle_{\chi\mathrm{PT}}. \tag{12}$$

In QCD, the axial current is simply given by

$$A_\mu^{a(\mathrm{QCD})} = \bar{q}\frac{\tau^a}{2}\gamma_\mu\gamma_5 q. \tag{13}$$

To derive the expression for the axial current in heavy-hadron chiral perturbation theory, one can use the

Noether procedure. For an infinitesimal local axial transformation,

$$R(x) = L^\dagger(x) = 1 + i\alpha_a(x)\tau^a, \tag{14}$$

one finds that the change in the leading-order Lagrangian is given by

$$\delta\mathcal{L} = (\partial^\mu \alpha_a) A_\mu^{a(\chi\mathrm{PT})} \tag{15}$$

with

$$\begin{aligned} A_\mu^{a(\chi\mathrm{PT})} = {} & \frac{if^2}{8}[\tau^a\Sigma^\dagger\partial_\mu\Sigma + \tau^a(\partial_\mu\Sigma)\Sigma^\dagger - \tau^a\Sigma\partial_\mu\Sigma^\dagger - \tau^a(\partial_\mu\Sigma^\dagger)\Sigma]^i{}_i - v_\mu \,\mathrm{tr}_\mathrm{D}[\bar{H}_i(\tau^a_{\xi-})^i{}_j H^j] - v_\mu[\bar{S}^\nu_{ij}(\tau^a_{\xi-})^i{}_k S^{kj}_\nu \\ & + \bar{S}^\nu_{ij}(\tau^a_{\xi-})^j{}_k S^{ik}_\nu] + v_\mu[\bar{T}_{ij}(\tau^a_{\xi-})^i{}_k T^{kj} + \bar{T}_{ij}(\tau^a_{\xi-})^j{}_k T^{ik}] + g_1\,\mathrm{tr}_\mathrm{D}[\bar{H}_i(\tau^a_{\xi+})^i{}_j\gamma_\mu\gamma_5 H^j] \\ & - ig_2\varepsilon_{\mu\nu\sigma\lambda}\bar{S}^\nu_{ki}v^\sigma(\tau^a_{\xi+})^i{}_j(S^\lambda)^{jk} + \sqrt{2}g_3[(\bar{S}_\mu)_{ki}(\tau^a_{\xi+})^i{}_j T^{jk} + \bar{T}_{ki}(\tau^a_{\xi+})^i{}_j(S_\mu)^{jk}], \end{aligned} \tag{16}$$

where we have introduced the quantities

$$\begin{aligned} \tau^a_{\xi-} &= \frac{1}{2}(\xi^\dagger\tau^a\xi - \xi\tau^a\xi^\dagger), \\ \tau^a_{\xi+} &= \frac{1}{2}(\xi^\dagger\tau^a\xi + \xi\tau^a\xi^\dagger). \end{aligned} \tag{17}$$

Equation (16) is the leading-order axial current in the chiral effective theory. In the following, we work with a particular flavor of the axial current,

$$A_\mu^{-(\chi\mathrm{PT})} = A_\mu^{1(\chi\mathrm{PT})} - iA_\mu^{2(\chi\mathrm{PT})}, \tag{18}$$

which corresponds to the QCD current $\bar{d}\gamma_\mu\gamma_5 u$. To lowest order in the pion fields (zero pion fields), the part of the axial current that will contribute to the matrix elements we will consider reads

$$\begin{aligned} A^{\mu-(\chi\mathrm{PT})} = {} & g_1\,\mathrm{tr}_\mathrm{D}[\bar{H}_d\gamma^\mu\gamma_5 H^u] - ig_2\varepsilon^{\mu\nu\sigma\lambda}v_\sigma[(\bar{S}_\nu)_{dd}(S_\lambda)^{du} \\ & + (\bar{S}_\nu)_{du}(S_\lambda)^{uu}] + \sqrt{2}g_3[-\bar{S}^\mu_{dd}T^{du} - \bar{T}_{du}(S^\mu)^{uu}]. \end{aligned} \tag{19}$$

We will now calculate matrix elements of (19) at leading order. To this end, we canonically quantize heavy-hadron chiral perturbation theory. The following derivation allows us to determine the correct normalization of the matrix elements (canonical quantization cannot be performed in the partially quenched theory, but the normalizations can be inferred). We begin with the heavy mesons. Using Eq. (1), we find that the free part of the heavy-meson-kinetic term in Eq. (8) is equal to

$$\begin{aligned} \mathcal{L}_H &= -iv_\mu\,\mathrm{tr}_\mathrm{D}[\bar{H}_i\partial^\mu H^i] \\ &= -iv_\mu[-2P_i^\dagger\partial^\mu P^i + 2P^{*\nu\dagger}_i\partial^\mu P^{*i}_\nu]. \end{aligned} \tag{20}$$

From this, we deduce the canonical equal-time commutation relations for the field operators (in the following, we use sans-serif font for operators)

$$\begin{aligned} [\mathsf{P}^i(\mathbf{x},t), \mathsf{P}^\dagger_j(\mathbf{x}',t)] &= \frac{1}{2v^0}\delta^i{}_j\delta^3(\mathbf{x}-\mathbf{x}'), \\ [\mathsf{P}^{*i}_\mu(\mathbf{x},t), \mathsf{P}^{*\nu\dagger}_j(\mathbf{x}',t)] &= -\frac{1}{2v^0}\delta^i{}_j(g_\mu{}^\nu - v_\mu v^\nu)\delta^3(\mathbf{x}-\mathbf{x}'). \end{aligned} \tag{21}$$

The field operators of the noninteracting theory can be written as

$$\begin{aligned} \mathsf{P}^i(x) &= \frac{1}{\sqrt{2v^0}}\int\frac{d^3k}{(2\pi)^3}\mathsf{a}^i_{(P)}(\mathbf{k})e^{-ik\cdot x}, \\ \mathsf{P}^\dagger_i(x) &= \frac{1}{\sqrt{2v^0}}\int\frac{d^3k}{(2\pi)^3}\mathsf{a}^{(P)\dagger}_i(\mathbf{k})e^{ik\cdot x}, \\ \mathsf{P}^{*i}_\mu(x) &= \frac{1}{\sqrt{2v^0}}\int\frac{d^3k}{(2\pi)^3}\sum_{s=1}^3\mathsf{a}^i_{(P^*)}(\mathbf{k},s)\epsilon_\mu(s)e^{-ik\cdot x}, \\ \mathsf{P}^{*\mu\dagger}_i(x) &= \frac{1}{\sqrt{2v^0}}\int\frac{d^3k}{(2\pi)^3}\sum_{s=1}^3\mathsf{a}^{(P^*)\dagger}_i(\mathbf{k},s)\epsilon^{*\mu}(s)e^{ik\cdot x}, \end{aligned} \tag{22}$$

where $k_0 = \mathbf{v}\cdot\mathbf{k}$, and the basis polarization vectors satisfy the spin sum

$$\sum_{s=1}^3\epsilon_\mu(s)\epsilon^*_\nu(s) = -g_{\mu\nu} + v_\mu v_\nu. \tag{23}$$

Equation (21) is satisfied if the commutation relations for the creation and annihilation operators are

$$\begin{aligned} [\mathsf{a}^i_{(P)}(\mathbf{k}), \mathsf{a}^{(P)\dagger}_j(\mathbf{k}')] &= (2\pi)^3\delta^i{}_j\delta^3(\mathbf{k}-\mathbf{k}'), \\ [\mathsf{a}^i_{(P^*)}(\mathbf{k},s), \mathsf{a}^{(P^*)\dagger}_j(\mathbf{k}',s')] &= (2\pi)^3\delta^i{}_j\delta_{ss'}\delta^3(\mathbf{k}-\mathbf{k}'). \end{aligned} \tag{24}$$

We define single-particle states via

$$\begin{aligned} |P^i(\mathbf{k})\rangle &= \sqrt{2v^0}\mathsf{a}^{(P)\dagger}_i(\mathbf{k})|0\rangle, \\ |P^{*i}(\mathbf{k},s)\rangle &= \sqrt{2v^0}\mathsf{a}^{(P^*)\dagger}_i(\mathbf{k},s)|0\rangle. \end{aligned} \tag{25}$$

Note that all the heavy-hadron states and operators also depend on the velocity v, which is a parameter in the

Lagrangian. However, since v is fixed throughout this paper, we do not include a label v explicitly.

The states (25) are normalized as

$$\langle P^i(\mathbf{k})|P^j(\mathbf{k}')\rangle = 2v^0(2\pi)^3\delta^{ij}\delta^3(\mathbf{k}-\mathbf{k}'),$$
$$\langle P^{*i}(\mathbf{k},s)|P^{*j}(\mathbf{k}',s')\rangle = 2v^0(2\pi)^3\delta^{ij}\delta_{ss'}\delta^3(\mathbf{k}-\mathbf{k}'). \tag{26}$$

We now calculate the matrix element $\langle P^{*d}|\mathsf{A}^{\mu-(\chi\mathrm{PT})}|P^u\rangle$. Expressing the mesonic part of the current (19) using the P and P^* fields, we find

$$\begin{aligned} A^{\mu-(\chi\mathrm{PT})} &= g_1\,\mathrm{tr}_\mathrm{D}[\bar H_d\gamma^\mu\gamma_5 H^u]+\ldots \\ &= g_1\,\mathrm{tr}_\mathrm{D}\left[P^{*\dagger}_{d\nu}\gamma^\nu\gamma^\mu\gamma_5(-P^u\gamma_5)\frac{1-\not v}{2}\right]+\ldots \\ &= -2g_1P^{*\mu\dagger}_d P^u+\ldots, \end{aligned} \tag{27}$$

where we have only shown the piece that contributes to the matrix element considered here. By inserting the field operators (22) into Eq. (27), we immediately obtain, at zero residual momentum,

$$\langle P^{*d}(0,s)|\mathsf{A}^{-(\chi\mathrm{PT})}_\mu(0)|P^u(0)\rangle|_\mathrm{LO} = -2g_1\varepsilon^*_\mu(s). \tag{28}$$

Next, we consider the $s_l=1$ baryon field S^{ij}_μ, for which the free part of the kinetic term in Eq. (8) is equal to

$$\begin{aligned} \mathcal{L}_S &= \bar S^\nu_{ij}[-iv_\mu\partial^\mu+\Delta]S^{ij}_\nu \\ &= \sum_{i\geq j}(2-\delta_{ij})\bar S^\nu_{ij}[-iv_\mu\partial^\mu+\Delta]S^{ij}_\nu. \end{aligned} \tag{29}$$

In the following we always assume that the flavor indices on the fields S^{ij} and $\bar S_{ij}$ are ordered as $i\geq j$. We find the canonical anticommutation relations

$$\begin{aligned} \{\mathsf{S}^{\mu ij}(\mathbf{x},t)_\alpha,\bar{\mathsf{S}}_{\nu kl\beta}(\mathbf{x}',t)\} = &-\frac{1}{(2-\delta_{ij})v^0}\delta^i{}_k\delta^j{}_l\left(\frac{1+\not v}{2}\right)_{\alpha\beta} \\ &\times(g^\mu{}_\nu-v^\mu v_\nu)\delta^3(\mathbf{x}-\mathbf{x}'). \end{aligned} \tag{30}$$

The field operators can be written as

$$\begin{aligned} \mathsf{S}^{\mu ij}(x) &= \frac{1}{\sqrt{(2-\delta_{ij})v^0}}\int\frac{d^3k}{(2\pi)^3} \\ &\quad\times\sum_{s=1}^6\mathsf{a}^{ij}_{(S)}(\mathbf{k},s)U^\mu(s)e^{-ik\cdot x}, \\ \bar{\mathsf{S}}_{\mu ij}(x) &= \frac{1}{\sqrt{(2-\delta_{ij})v^0}}\int\frac{d^3k}{(2\pi)^3} \\ &\quad\times\sum_{s=1}^6\mathsf{a}^{(S)\dagger}_{ij}(\mathbf{k},s)\bar U_\mu(s)e^{ik\cdot x}, \end{aligned} \tag{31}$$

where $k_0=\mathbf{v}\cdot\mathbf{k}+\frac{1}{v^0}\Delta$, and the basis spinors satisfy the spin sum

$$\sum_{s=1}^6 U^\mu_\alpha(s)\bar U^\nu_\beta(s) = -(g^{\mu\nu}-v^\mu v^\nu)\left[\frac{1+\not v}{2}\right]_{\alpha\beta}. \tag{32}$$

Note that $U_\mu(s)$ is *not* a Rarita-Schwinger spinor, but rather contains the degrees of freedom of both spin-1/2 and spin-3/2 baryons. The creation and annihilation operators satisfy the anticommutation relations

$$\{\mathsf{a}^{ij}_{(S)}(\mathbf{k},s),\mathsf{a}^{(S)\dagger}_{kl}(\mathbf{k}',s')\} = (2\pi)^3\delta^i{}_k\delta^j{}_l\delta_{ss'}\delta^3(\mathbf{k}-\mathbf{k}'). \tag{33}$$

Here we define single-particle states via

$$|S^{ij}(\mathbf{k},s)\rangle = \sqrt{v^0}\mathsf{a}^{(S)\dagger}_{ij}(\mathbf{k},s)|0\rangle, \tag{34}$$

which corresponds to the following normalization:

$$\langle S^{ij}(\mathbf{k},s)|S^{kl}(\mathbf{k}',s')\rangle = v^0(2\pi)^3\delta^{ik}\delta^{jl}\delta_{ss'}\delta^3(\mathbf{k}-\mathbf{k}'). \tag{35}$$

Using the expression (19) for the axial current, and the mode decomposition (31), we find the following leading-order matrix element of the axial current:

$$\begin{aligned} &\langle S^{dd}(0,s)|\mathsf{A}^{\mu-(\chi\mathrm{PT})}(0)|S^{du}(0,s')\rangle|_\mathrm{LO} \\ &\quad= -\frac{i}{\sqrt{2}}g_2v_\lambda\epsilon^{\lambda\mu\nu\rho}\bar U_\nu(s)U_\rho(s'). \end{aligned} \tag{36}$$

Finally, we consider the $s_l=0$ baryon field T^{ij}. The free part of the kinetic term in Eq. (8) is equal to

$$\mathcal{L}_T = iv_\mu\bar T_{ij}\partial^\mu T^{ij} = 2iv_\mu\sum_{i>j}\bar T_{ij}\partial^\mu T^{ij}. \tag{37}$$

For the T and $\bar T$ fields, we also assume in the following that the flavor indices are ordered ($i>j$). We obtain the canonical anticommutation relations

$$\{\mathsf{T}^{ij}(\mathbf{x},t)_\alpha,\bar{\mathsf{T}}_{kl\beta}(\mathbf{x}',t)\} = \frac{1}{2v^0}\delta^i{}_k\delta^j{}_l\left(\frac{1+\not v}{2}\right)_{\alpha\beta}\delta^3(\mathbf{x}-\mathbf{x}'), \tag{38}$$

and the field operators can be written as

$$\begin{aligned} \mathsf{T}^{ij}(x) &= \frac{1}{\sqrt{2v^0}}\int\frac{d^3k}{(2\pi)^3}\sum_{s=1}^2\mathsf{a}^{ij}_{(T)}(\mathbf{k},s)\mathcal{U}(s)e^{-ik\cdot x}, \\ \bar{\mathsf{T}}_{ij}(x) &= \frac{1}{\sqrt{2v^0}}\int\frac{d^3k}{(2\pi)^3}\sum_{s=1}^2\mathsf{a}^{(T)}_{ij}(\mathbf{k},s)\bar{\mathcal{U}}(s)e^{ik\cdot x}, \end{aligned} \tag{39}$$

where $k_0=\mathbf{v}\cdot\mathbf{k}$, and the basis spinors satisfy the spin sum

$$\sum_{s=1}^2\mathcal{U}_\alpha(s)\bar{\mathcal{U}}_\beta(s) = \left[\frac{1+\not v}{2}\right]_{\alpha\beta}. \tag{40}$$

The creation and annihilation operators satisfy the anticommutation relations

$$\{\mathsf{a}^{ij}_{(T)}(\mathbf{k}, s), \mathsf{a}^{(T)\dagger}_{kl}(\mathbf{k}', s')\} = (2\pi)^3 \delta^i{}_k \delta^j{}_l \delta_{ss'} \delta^3(\mathbf{k} - \mathbf{k}'). \tag{41}$$

Again, we define single-particle states via

$$|T^{ij}(\mathbf{k}, s)\rangle = \sqrt{v^0}\,\mathsf{a}^{(T)\dagger}_{ij}(\mathbf{k}, s)|0\rangle, \tag{42}$$

which are normalized as

$$\langle T^{ij}(\mathbf{k}, s)|T^{kl}(\mathbf{k}', s')\rangle = v^0 (2\pi)^3 \delta^{ik}\delta^{jl}\delta_{ss'}\delta^3(\mathbf{k} - \mathbf{k}'). \tag{43}$$

Now we have all the ingredients to obtain the leading-order S-T transition matrix element of the axial current:

$$\langle S^{dd}(0, s)|\mathsf{A}^{\mu-(\chi\mathrm{PT})}(0)|T^{du}(0, s')\rangle|_{\mathrm{LO}} = -g_3 \bar{U}^\mu(s)\mathcal{U}(s'). \tag{44}$$

To go beyond leading order, we need to replace g_1, g_2, g_3 in Eqs. (28), (36), and (44) by "effective axial couplings" $(g_1)_{\mathrm{eff}}$, $(g_2)_{\mathrm{eff}}$, and $(g_3)_{\mathrm{eff}}$,

$$\begin{aligned}
&\langle P^{*d}(0, s)|\mathsf{A}^{\mu-(\chi\mathrm{PT})}(0)|P^u(0)\rangle = -2(g_1)_{\mathrm{eff}}\varepsilon^{*\mu}(s),\\
&\langle S^{dd}(0, s)|\mathsf{A}^{\mu-(\chi\mathrm{PT})}(0)|S^{du}(0, s')\rangle\\
&\quad = -\frac{i}{\sqrt{2}}(g_2)_{\mathrm{eff}} v_\lambda \epsilon^{\lambda\mu\nu\rho}\bar{U}_\nu(s)U_\rho(s'),\\
&\langle S^{dd}(0, s)|\mathsf{A}^{\mu-(\chi\mathrm{PT})}(0)|T^{du}(0, s')\rangle = -(g_3)_{\mathrm{eff}}\bar{U}^\mu(s)\mathcal{U}(s').
\end{aligned} \tag{45}$$

The next-to-leading-order expressions in the partially quenched $SU(4|2)$ theory (for $m_u^{(\mathrm{val})} = m_d^{(\mathrm{val})}$ and $m_u^{(\mathrm{sea})} = m_d^{(\mathrm{sea})}$), calculated via the perturbative expansion of the path integral, have been derived in Ref. [20] and are given by

$$\begin{aligned}
(g_1)_{\mathrm{eff}} &= g_1 - \frac{2g_1}{f^2}\mathcal{I}(m_\pi^{(\mathrm{vs})}) + \frac{g_1^3}{f^2}[4\mathcal{H}(m_\pi^{(\mathrm{vs})}, 0) - 4\delta_{VS}^2\mathcal{H}_{\eta'}(m_\pi^{(\mathrm{vv})}, 0)] + (\text{analytic terms}),\\
(g_2)_{\mathrm{eff}} &= g_2 - \frac{2g_2}{f^2}\mathcal{I}(m_\pi^{(\mathrm{vs})}) + \frac{g_2^3}{f^2}\left[\frac{3}{2}\mathcal{H}(m_\pi^{(\mathrm{vs})}, 0) - \delta_{VS}^2\mathcal{H}_{\eta'}(m_\pi^{(\mathrm{vv})}, 0)\right] + \frac{g_2 g_3^2}{f^2}[2\mathcal{H}(m_\pi^{(\mathrm{vs})}, -\Delta) - \mathcal{H}(m_\pi^{(\mathrm{vv})}, -\Delta)\\
&\quad - 2\mathcal{K}(m_\pi^{(\mathrm{vs})}, -\Delta, 0)] + (\text{analytic terms}),\\
(g_3)_{\mathrm{eff}} &= g_3 - \frac{2g_3}{f^2}\mathcal{I}(m_\pi^{(\mathrm{vs})}) + \frac{g_3^3}{f^2}\left[\mathcal{H}(m_\pi^{(\mathrm{vs})}, -\Delta) - \frac{1}{2}\mathcal{H}(m_\pi^{(\mathrm{vv})}, -\Delta) + \frac{3}{2}\mathcal{H}(m_\pi^{(\mathrm{vv})}, \Delta) + 3\mathcal{H}(m_\pi^{(\mathrm{vs})}, \Delta) - \mathcal{K}(m_\pi^{(\mathrm{vs})}, \Delta, 0)\right]\\
&\quad + \frac{g_3 g_2^2}{f^2}[-\mathcal{H}(m_\pi^{(\mathrm{vs})}, \Delta) - \mathcal{H}(m_\pi^{(\mathrm{vv})}, \Delta) + \mathcal{H}(m_\pi^{(\mathrm{vs})}, 0) - \delta_{VS}^2\mathcal{H}_{\eta'}(m_\pi^{(\mathrm{vv})}, 0)] + (\text{analytic terms}).
\end{aligned} \tag{46}$$

Here, $m_\pi^{(\mathrm{vs})}$ denotes the mass of a pion consisting of a valence and a sea quark, $m_\pi^{(\mathrm{vv})}$ denotes the mass of a pion consisting of two valence quarks, and $\delta_{VS}^2 = [m_\pi^{(\mathrm{vv})}]^2 - [m_\pi^{(\mathrm{vs})}]^2$. The functions $\mathcal{I}$, $\mathcal{H}$, $\mathcal{H}_{\eta'}$ and $\mathcal{K}$, which arise from the chiral loops and include the leading effects of the finite spatial volume, are defined in Ref. [20]. At the order considered here, the analytic terms in Eq. (46) are linear functions of $[m_\pi^{(\mathrm{vv})}]^2$ and $[m_\pi^{(\mathrm{vs})}]^2$.

C. Axial-current matrix elements in lattice QCD

For the lattice QCD calculation, we construct interpolating fields for the heavy hadrons in terms of the quark fields as follows:

$$\begin{aligned}
P^i &= \bar{Q}_{a\alpha}(\gamma_5)_{\alpha\beta}\tilde{q}^i_{a\beta}, \qquad P^{*i}_\mu = \bar{Q}_{a\alpha}(\gamma_\mu)_{\alpha\beta}\tilde{q}^i_{a\beta},\\
S^{ij}_{\mu\alpha} &= \epsilon_{abc}(C\gamma_\mu)_{\beta\gamma}\tilde{q}^i_{a\beta}\tilde{q}^j_{b\gamma}Q_{c\alpha},\\
T^{ij}_\alpha &= \epsilon_{abc}(C\gamma_5)_{\beta\gamma}\tilde{q}^i_{a\beta}\tilde{q}^j_{b\gamma}Q_{c\alpha}.
\end{aligned} \tag{47}$$

Here, a, b, c are color indices, and α, β, γ are spinor indices. The light-quark field of flavor i is denoted by q^i (we will also use the notation $u = q^u$, $d = q^d$), and the heavy-quark (antiquark) field is denoted by Q ($\bar{Q}$). The tilde on the light-quark fields indicates that these are smeared over multiple spatial lattice sites, in order to improve the overlap of the interpolating fields with the corresponding ground-state hadrons and reduce excited-state contamination. We use gauge-invariant Gaussian smearing obtained by

$$\tilde{q} = \left(1 + \frac{\sigma^2}{4n_S}\Delta^{(2)}\right)^{n_S} q, \tag{48}$$

where $\Delta^{(2)}$ is a three-dimensional gauge-covariant lattice Laplacian which includes gauge links, σ is the smearing width and n_S is the number of smearing iterations.

The heavy quark Q is defined in the static limit, and we set $\mathbf{v} = 0$. The static heavy-quark field Q satisfies

$$\frac{1 + \gamma^0}{2}Q = Q. \tag{49}$$

Note that the interpolating field $S^{ij}_{\mu\alpha}$ couples to both the $J = 1/2$ and the $J = 3/2$ baryons with $s_l = 1$, with exactly the same relative amplitudes as (3).

We use the local four-dimensional lattice axial current, where the quark and antiquark fields are evaluated at the same lattice point. This current requires a finite renormalization factor Z_A to match the continuum QCD current,

$$A_\mu^{a(\mathrm{LQCD})} = Z_A \bar{q}_{ia\alpha} \frac{1}{2} (\tau^a)^i{}_j (\gamma_\mu \gamma_5)_{\alpha\beta} q^j_{a\beta}. \tag{50}$$

The value of Z_A depends on the lattice action used, as well as the lattice spacing. We will come back to this in Sec. III. As before, we will work with a specific flavor of the axial current,

$$A_\mu^{-(\mathrm{LQCD})} = Z_A \bar{d}_{a\alpha} (\gamma_\mu \gamma_5)_{\alpha\beta} u_{a\beta}. \tag{51}$$

In the following, we will omit the superscript "-(LQCD)" in the axial current (51). Next, we define the overlap factors, which describe the overlap of the operators corresponding to the interpolating fields (47) with the relevant ground-state hadrons in QCD. Here, we use the same notation and normalization of states as in Sec. II B,

$$\begin{aligned}
\langle 0|\mathsf{P}^i(0)|P^i(k)\rangle &= Z_{P^i}, \\
\langle 0|\mathsf{P}^{*i}_\mu(0)|P^{*i}(\mathbf{k}, s)\rangle &= Z_{P^{*i}} \varepsilon_\mu(s), \\
\langle 0|\mathsf{S}^{ij}_{\mu\alpha}(0)|S^{ij}(\mathbf{k}, s)\rangle &= Z_{S^{ij}} U_{\mu\alpha}(s), \\
\langle 0|\mathsf{T}^{ij}_\alpha(0)|T^{ij}(\mathbf{k}, s)\rangle &= Z_{T^{ij}} \mathcal{U}_\alpha(s).
\end{aligned} \tag{52}$$

We stress that these states are now meant to be hadron states in (lattice) QCD, rather than in the chiral effective theory.

We calculate Euclidean two-point functions of the interpolating fields (47), as well as Euclidean three-point functions with an insertion of the axial current (51). These Euclidean correlation functions are obtained from the lattice path integral, which is performed numerically using importance sampling. In the following, we assume that the Wick rotation $t \to -it$ has been performed, so that t denotes the Euclidean time.

We calculate the following three-point functions, where $\langle \ldots \rangle$ denotes the path-integral over the gauge and fermion fields (for the domain-wall action used in this work, there is also an additional path integral over Pauli-Villars fields [25,32]),

$$\begin{aligned}
C[P^{*d} A P_u^\dagger]^{\mu\nu}(t, t') &= \sum_{\mathbf{x}} \sum_{\mathbf{x}'} \langle P^{*d\mu}(\mathbf{x}, t) A^\nu(\mathbf{x}', t') P_u^\dagger(0)\rangle, \\
C[S^{dd} A \bar{S}_{du}]^{\mu\nu\rho}_{\alpha\beta}(t, t') &= \sum_{\mathbf{x}} \sum_{\mathbf{x}'} \langle S^{dd\mu}_\alpha(\mathbf{x}, t) A^\nu(\mathbf{x}', t') \bar{S}^\rho_{du\beta}(0)\rangle, \\
C[S^{dd} A \bar{T}_{du}]^{\mu\nu}_{\alpha\beta}(t, t') &= \sum_{\mathbf{x}} \sum_{\mathbf{x}'} \langle S^{dd\mu}_\alpha(\mathbf{x}, t) A^\nu(\mathbf{x}', t') \bar{T}_{du\beta}(0)\rangle, \\
C[T^{du} A^\dagger \bar{S}_{dd}]^{\mu\nu}_{\alpha\beta}(t, t') &= \sum_{\mathbf{x}} \sum_{\mathbf{x}'} \langle T^{du}_\alpha(\mathbf{x}, t) A^{\mu\dagger}(\mathbf{x}', t') \bar{S}^\nu_{dd\beta}(0)\rangle.
\end{aligned} \tag{53}$$

In addition, we calculate the two-point functions

$$\begin{aligned}
C[P^u P_u^\dagger](t) &= \sum_{\mathbf{x}} \langle P^u(\mathbf{x}, t) P_u^\dagger(0)\rangle, \\
C[P^{*d} P_d^{*\dagger}]^{\mu\nu}(t) &= \sum_{\mathbf{x}} \langle P^{*d\mu}(\mathbf{x}, t) P_d^{*\nu\dagger}(0)\rangle, \\
C[S^{dd} \bar{S}_{dd}]^{\mu\nu}_{\alpha\beta}(t) &= \sum_{\mathbf{x}} \langle S^{dd\mu}_\alpha(\mathbf{x}, t) \bar{S}^\nu_{dd\beta}(0)\rangle, \\
C[S^{du} \bar{S}_{du}]^{\mu\nu}_{\alpha\beta}(t) &= \sum_{\mathbf{x}} \langle S^{du\nu}_\alpha(\mathbf{x}, t) \bar{S}^\nu_{du\beta}(0)\rangle, \\
C[T^{du} \bar{T}_{du}]_{\alpha\beta}(t) &= \sum_{\mathbf{x}} \langle T^{du}_\alpha(\mathbf{x}, t) \bar{T}_{du\beta}(0)\rangle.
\end{aligned} \tag{54}$$

As an example, we show how the two-point function $C[S^{dd} \bar{S}_{dd}]^{\mu\nu}_{\alpha\beta}(t)$ is constructed in terms of quark propagators. The lattice calculation is performed in the isospin limit of equal up and down quark masses. Inserting the definitions of the interpolating fields, and performing the Grassmann integrals over the fermion fields explicitly, we have

$$\begin{aligned}
C[S^{dd} \bar{S}_{dd}]^{\mu\nu}_{\alpha\beta}(t) &= \epsilon_{abc} (C\gamma^\mu)_{\delta\gamma} \epsilon_{fgh} (\overline{C\gamma^\nu})_{\rho\sigma} \sum_{\mathbf{x}} \langle \tilde{d}^a_\delta(x) \tilde{d}^b_\gamma(x) Q^c_\alpha(x) \bar{\tilde{d}}^g_\rho(0) \bar{\tilde{d}}^f_\sigma(0) \bar{Q}^h_\beta(0)\rangle \\
&= \epsilon_{abc} (C\gamma^\mu)_{\delta\gamma} \epsilon_{fgh} (\overline{C\gamma^\nu})_{\rho\sigma} \sum_{\mathbf{x}} \langle \tilde{\tilde{G}}^{af}_{(q)\delta\sigma}(x, 0) \tilde{\tilde{G}}^{bg}_{(q)\gamma\rho}(x, 0) G^{ch}_{(Q)\alpha\beta}(x, 0) \\
&\quad - \tilde{\tilde{G}}^{ag}_{(q)\delta\rho}(x, 0) \tilde{\tilde{G}}^{bf}_{(q)\gamma\sigma}(x, 0) G^{ch}_{(Q)\alpha\beta}(x, 0)\rangle_U \\
&= 2\epsilon_{abc} (C\gamma^\mu)_{\delta\gamma} \epsilon_{fgh} (\overline{C\gamma^\nu})_{\rho\sigma} \sum_{\mathbf{x}} \langle \tilde{\tilde{G}}^{af}_{(q)\delta\sigma}(x, 0) \tilde{\tilde{G}}^{bg}_{(q)\gamma\rho}(x, 0) G^{ch}_{(Q)\alpha\beta}(x, 0)\rangle_U.
\end{aligned} \tag{55}$$

Here, $\tilde{\tilde{G}}_{(q)}$ denotes a smeared-source smeared-sink light-quark propagator and $G_{(Q)}$ a heavy-quark propagator. The notation $\langle \ldots \rangle_U$ indicates the path integral over the gauge fields U only. In the last step in Eq. (55) we have used the symmetry of $(C\gamma_\mu)$ and the antisymmetry of ϵ_{abc} to equate the two Wick contractions. Note that the two-point function $C[S^{du} \bar{S}_{du}]^{\mu\nu}_{\alpha\beta}(t)$ contains only one Wick contraction, because the two light quarks have different flavors. Therefore, in the isospin limit,

$$C[S^{du} \bar{S}_{du}]^{\mu\nu}_{\alpha\beta}(t) = \frac{1}{2} C[S^{dd} \bar{S}_{dd}]^{\mu\nu}_{\alpha\beta}(t). \tag{56}$$

For the static lattice action we are using, the heavy-quark propagator is equal to

$$G_{(Q)\alpha\beta}(x,0) = \delta_{\mathbf{x},\mathbf{0}}\left[\frac{1+\gamma^0}{2}\right]_{\alpha\beta}\tilde{U}_0^\dagger(\mathbf{x},t-a) \times \tilde{U}_0^\dagger(\mathbf{x},t-2a)\ldots\tilde{U}_0^\dagger(\mathbf{x},0), \quad (57)$$

where $\tilde{U}_0$ is a spatially smeared gauge link in the temporal direction (more details will be given in Sec. III). Because the static heavy-quark propagator (57) contains the Kronecker delta $\delta_{\mathbf{x},\mathbf{0}}$, the sums over $\mathbf{x}$ in all the correlation functions, Eqs. (53) and (54), are eliminated. To calculate the three-point functions (53) in terms of quark propagators, we use pairs of light-quark propagators with smeared sources at (0, 0) and (0, t). This means that new inversions are needed for each value of t.

By using the Hamiltonian and the momentum operator to shift the left interpolating operator from x to 0 and the axial current from x' to 0, and inserting complete sets of states, we can show that

$$\begin{aligned}
C[P^{*d}AP_u^\dagger]^{\mu\nu}(t,t') &= \frac{1}{4}Z_{P^{*d}}Z_{P^u}^*\sum_{s=1}^{3}\varepsilon^\mu(s)\langle P^{*d}(0,s)|\mathsf{A}^\nu(0)|P^\mu(0)\rangle e^{-E_{P^{*d}}(t-t')}e^{-E_{P^u}t'}+\ldots,\\
C[S^{dd}A\bar{S}_{du}]^{\mu\nu\rho}_{\alpha\beta}(t,t') &= Z_{S^{dd}}Z_{S^{du}}^*\sum_{s=1}^{6}\sum_{s'=1}^{6}U_\alpha^\mu(s)\langle S^{dd}(0,s)|\mathsf{A}^\nu(0)|S^{du}(0,s')\rangle\bar{U}_\beta^\rho(s')e^{-E_{S^{dd}}(t-t')}e^{-E_{S^{du}}t'}+\ldots,\\
C[S^{dd}A\bar{T}_{du}]^{\mu\nu}_{\alpha\beta}(t,t') &= Z_{S^{dd}}Z_{T^{du}}^*\sum_{s=1}^{6}\sum_{s'=1}^{2}U_\alpha^\mu(s)\langle S^{dd}(0,s)|\mathsf{A}^\nu(0)|T^{du}(0,s')\rangle\bar{\mathcal{U}}_\beta(s')e^{-E_{S^{dd}}(t-t')}e^{-E_{T^{du}}t'}+\ldots,\\
C[T^{du}A^\dagger\bar{S}_{dd}]^{\mu\nu}_{\alpha\beta}(t,t') &= Z_{T^{du}}Z_{S^{dd}}^*\sum_{s=1}^{2}\sum_{s'=1}^{6}\mathcal{U}_\alpha(s)\langle T^{du}(0,s)|\mathsf{A}^{\mu\dagger}(0)|S^{dd}(0,s')\rangle\bar{U}_\beta^\nu(s')e^{-E_{T^{du}}(t-t')}e^{-E_{S^{dd}}t'}+\ldots
\end{aligned} \quad (58)$$

and

$$\begin{aligned}
C[P^uP_u^\dagger](t) &= \frac{1}{2}|Z_{P^u}|^2e^{-E_{P_u}t}+\ldots, \qquad C[P^{*d}P_d^{*\dagger}]^{\mu\nu}(t) = \frac{1}{2}|Z_{P^{*d}}|^2\sum_{s=1}^{3}\varepsilon^\mu(s)\varepsilon^{*\nu}(s)e^{-E_{P^{*d}}t}+\ldots,\\
C[S^{dd}\bar{S}_{dd}]^{\mu\nu}_{\alpha\beta}(t) &= \sum_{s=1}^{6}U_\alpha^\mu(s)\bar{U}_\beta^\nu(s)|Z_{S^{dd}}|^2e^{-E_{S^{dd}}t}+\ldots, \qquad C[S^{du}\bar{S}_{du}]^{\mu\nu}_{\alpha\beta}(t) = \sum_{s=1}^{6}U_\alpha^\mu(s)\bar{U}_\beta^\nu(s)|Z_{S^{du}}|^2e^{-E_{S^{du}}t}+\ldots,\\
C[T^{du}\bar{T}_{du}]_{\alpha\beta}(t) &= \sum_{s=1}^{2}\mathcal{U}_\alpha(s)\bar{\mathcal{U}}_\beta(s)|Z_{T^{du}}|^2e^{-E_{T^{du}}t}+\ldots,
\end{aligned} \quad (59)$$

where the ellipsis indicates contributions from excited states, whose contribution relative to the ground-state contribution shown here vanishes exponentially for $t\to\infty$, $t'\to\infty$, $t-t'\to\infty$ (here and in the following we assume an infinite temporal extent of the lattice). We will return to the discussion of excited states at the end of this section. Using the relations (23), (32), and (40) to perform the spin sums (recall that here we have $\mathbf{v}=0$) and Eq. (45) to express the axial-current matrix elements in terms of the effective axial couplings $(g_1)_{\text{eff}}$, $(g_2)_{\text{eff}}$, $(g_3)_{\text{eff}}$, we obtain

$$\begin{aligned}
C[P^{*d}AP_u^\dagger]^{\mu\nu}(t,t') &= -\frac{1}{2}(g_1)_{\text{eff}}(v^\mu v^\nu-g^{\mu\nu})Z_{P^{*d}}Z_{P^u}^*e^{-E_{P^{*d}}(t-t')}e^{-E_{P^u}t'}+\ldots,\\
C[S^{dd}A\bar{S}_{du}]^{\mu\nu\rho}_{\alpha\beta}(t,t') &= \frac{i}{\sqrt{2}}(g_2)_{\text{eff}}v_\lambda\epsilon^{\lambda\mu\nu\rho}\left[\frac{1+\gamma^0}{2}\right]_{\alpha\beta}Z_{S^{dd}}Z_{S^{du}}^*e^{-E_{S^{dd}}(t-t')}e^{-E_{S^{du}}t'}+\ldots,\\
C[S^{dd}A\bar{T}_{du}]^{\mu\nu}_{\alpha\beta}(t,t') &= -(g_3)_{\text{eff}}(v^\mu v^\nu-g^{\mu\nu})\left[\frac{1+\gamma^0}{2}\right]_{\alpha\beta}Z_{S^{dd}}Z_{T^{du}}^*e^{-E_{S^{dd}}(t-t')}e^{-E_{T^{du}}t'}+\ldots,\\
C[T^{du}A^\dagger\bar{S}_{dd}]^{\mu\nu}_{\alpha\beta}(t,t') &= -(g_3)_{\text{eff}}(v^\mu v^\nu-g^{\mu\nu})\left[\frac{1+\gamma^0}{2}\right]_{\alpha\beta}Z_{T^{du}}Z_{S^{dd}}^*e^{-E_{T^{du}}(t-t')}e^{-E_{S^{dd}}t'}+\ldots
\end{aligned} \quad (60)$$

and

$$
\begin{aligned}
&C[P^u P_u^\dagger](t) = \frac{1}{2}|Z_{P^u}|^2 e^{-E_{P^u} t} + \ldots, \qquad C[P^{*d} P_d^{*\dagger}]^{\mu\nu}(t) = \frac{1}{2}(v^\mu v^\nu - g^{\mu\nu})|Z_{P^{*d}}|^2 e^{-E_{P^{*d}} t} + \ldots, \\
&C[S^{dd}\bar{S}_{dd}]^{\mu\nu}_{\alpha\beta}(t) = (v^\mu v^\nu - g^{\mu\nu})\left[\frac{1+\gamma^0}{2}\right]_{\alpha\beta}|Z_{S^{dd}}|^2 e^{-E_{S^{dd}} t} + \ldots, \\
&C[S^{du}\bar{S}_{du}]^{\mu\nu}_{\alpha\beta}(t) = (v^\mu v^\nu - g^{\mu\nu})\left[\frac{1+\gamma^0}{2}\right]_{\alpha\beta}|Z_{S^{du}}|^2 e^{-E_{S^{du}} t} + \ldots, \\
&C[T^{du}\bar{T}_{du}]_{\alpha\beta}(t) = \left[\frac{1+\gamma^0}{2}\right]_{\alpha\beta}|Z_{T^{du}}|^2 e^{-E_{T^{du}} t} + \ldots.
\end{aligned} \tag{61}
$$

In the following, we remove the trivial spin-structure $[\frac{1+\gamma_0}{2}]_{\alpha\beta}$, which comes purely from the heavy-quark propagator (57), from all baryon correlation functions.

Because the lattice calculation is performed in the isospin limit (and in the static limit for the heavy quark), we have the relations

$$
\begin{aligned}
E_{P^u} &= E_{P^{d*}}, \qquad & Z_{P^u} &= Z_{P^{d*}}, \\
E_{S^{dd}} &= E_{S^{du}}, \qquad & Z_{S^{dd}} &= \sqrt{2} Z_{S^{du}}
\end{aligned} \tag{62}
$$

[the factor of $\sqrt{2}$ in the last line comes from Eq. (56)]. As a consequence of the equality of energies, the t' dependence of the ground-state contribution in the three-point functions $C[P^{*d} A P_u^\dagger]^{\mu\nu}(t, t')$ and $C[S^{dd} A \bar{S}_{du}]^{\mu\nu\rho}(t, t')$ cancels completely. For these three-point functions, the t dependence as well as the Z factors in the ground-state contribution can be canceled by forming the ratios

$$
R_1(t, t') = -\frac{\frac{1}{3}\sum_{\mu=1}^3 C[P^{*d} A P_u^\dagger]^{\mu\mu}(t, t')}{C[P^u P_u^\dagger](t)} = (g_1)_{\text{eff}} + \ldots, \tag{63}
$$

and

$$
\begin{aligned}
R_2(t, t') &= 2\frac{\frac{i}{6}\sum_{\mu,\nu,\rho=1}^3 \epsilon_{0\mu\nu\rho} C[S^{dd} A \bar{S}_{du}]^{\mu\nu\rho}(t, t')}{\frac{1}{3}\sum_{\mu=1}^3 C[S^{dd}\bar{S}_{dd}]^{\mu\mu}(t)} \\
&= (g_2)_{\text{eff}} + \ldots,
\end{aligned} \tag{64}
$$

where, as before, the ellipsis indicates contributions from excited states that vanish exponentially when all Euclidean time separations are taken to infinity. To extract $(g_3)_{\text{eff}}$, we use the double ratio

$$
R_3(t, t') = \sqrt{\frac{[\frac{1}{3}\sum_{\mu=1}^3 C[S^{dd} A \bar{T}_{du}]^{\mu\mu}(t, t')][\frac{1}{3}\sum_{\mu=1}^3 C[T^{du} A^\dagger \bar{S}_{dd}]^{\mu\mu}(t, t')]}{[\frac{1}{3}\sum_{\mu=1}^3 C[S^{dd}\bar{S}_{dd}]^{\mu\mu}(t)][C[T^{du}\bar{T}_{du}](t)]}} = (g_3)_{\text{eff}} + \ldots. \tag{65}
$$

The numerical results for (63)–(65) and the subsequent analysis will be described in Sec. IV. In the following, we discuss the contributions from excited states to the ratios. Again, we assume an infinite temporal extent of the lattice; with a finite temporal extent T this means that the following discussion is only valid for source-sink separations t that are smaller than $T/2$ by a sufficient distance (which is the case in our numerical calculations). We begin with R_1, and define

$$
\langle 0|\mathsf{P}^u(0)|P_n^u\rangle = Z_{P,n}, \qquad \langle 0|\mathsf{P}_\mu^{*d}(0)|P_n^{*d}(\varepsilon)\rangle = Z_{P,n}\varepsilon_\mu, \qquad \langle P_n^{*d}|\mathsf{A}_\mu(0)|P_m^u(\varepsilon)\rangle = -2A_{nm}^{(PP^*)}\varepsilon_\mu^*, \tag{66}
$$

where $|P_n^u\rangle$ denotes the nth excited state with a nonzero overlap $\langle 0|\mathsf{P}^u(0)|P_n^u\rangle$, and similarly for $|P_n^{*d}(\varepsilon)\rangle$. Because of heavy-quark symmetry and isospin symmetry, all energies and Z-factors in the P^u sector are equal to those in the P^{*d} sector, and $A_{nm}^{(PP^*)} = A_{mn}^{*(PP^*)}$. Note that

$$
A_{11}^{(PP^*)} = (g_1)_{\text{eff}}. \tag{67}
$$

The complete spectral decomposition of R_1 reads

$$
R_1(t, t') = \frac{\sum_{n=1}^\infty \sum_{m=1}^\infty Z_{P,n} Z_{P,m}^* A_{nm}^{(PP^*)} e^{-E_{P,n} t} e^{-E_{P,m}(t-t')}}{\sum_{n=1}^\infty |Z_{P,n}|^2 e^{-E_{P,n} t}}. \tag{68}
$$

Showing only the contributions from the ground states and first excited states, we find that

$$
R_1(t, t') = A_{11}^{(PP^*)} + \frac{\left|\frac{Z_{P,2}}{Z_{P,1}}\right|^2 (A_{22}^{(PP^*)} - A_{11}^{(PP^*)}) e^{-\delta_P t} + \frac{Z_{P,1} Z_{P,2}^*}{|Z_{P,1}|^2} A_{12}^{(PP^*)} e^{-\delta_P t'} + \frac{Z_{P,2} Z_{P,1}^*}{|Z_{P,1}|^2} A_{12}^{*(PP^*)} e^{-\delta_P (t-t')}}{1 + \left|\frac{Z_{P,2}}{Z_{P,1}}\right|^2 e^{-\delta_P t}} + \ldots, \tag{69}
$$

with the energy gap $\delta_P = E_{P,2} - E_{P,1}$. For a given value of t, the smallest contamination from excited states is obtained at the midpoint $t' = t/2$. Evaluating (69) at $t' = t/2$, we get

$$R_1(t, t/2) = A_{11}^{(PP^*)} + \frac{|\frac{Z_{P,2}}{Z_{P,1}}|^2 (A_{22}^{(PP^*)} - A_{11}^{(PP^*)}) e^{-\delta_P t} + 2\Re[\frac{Z_{P,1} Z_{P,2}^*}{|Z_{P,1}|^2} A_{12}^{(PP^*)}] e^{-(1/2)\delta_P t}}{1 + |\frac{Z_{P,2}}{Z_{P,1}}|^2 e^{-\delta_P t}} + \ldots, \tag{70}$$

where $\Re$ denotes the real part. By using the Taylor expansion $1/(1 + |\frac{Z_{P,2}}{Z_{P,1}}|^2 e^{-\delta_P t}) = 1 - |\frac{Z_{P,2}}{Z_{P,1}}|^2 e^{-\delta_P t} + \ldots$, we obtain

$$R_1(t, t/2) = A_{11}^{(PP^*)} + \left|\frac{Z_{P,2}}{Z_{P,1}}\right|^2 (A_{22}^{(PP^*)} - A_{11}^{(PP^*)}) e^{-\delta_P t} + 2\Re\left[\frac{Z_{P,1} Z_{P,2}^*}{|Z_{P,1}|^2} A_{12}^{(PP^*)}\right] e^{-(1/2)\delta_P t} + \ldots, \tag{71}$$

where we have omitted terms that decay like $e^{-(3/2)\delta_P t}$ or faster, and are therefore exponentially suppressed relative to the terms shown in (71) at large t. The result for $R_2(t, t/2)$ has the same form (with suitable definitions of the overlap factors and matrix elements):

$$R_2(t, t/2) = A_{11}^{(SS)} + \left|\frac{Z_{S,2}}{Z_{S,1}}\right|^2 (A_{22}^{(SS)} - A_{11}^{(SS)}) e^{-\delta_S t} + 2\Re\left[\frac{Z_{S,1} Z_{S,2}^*}{|Z_{S,1}|^2} A_{12}^{(SS)}\right] e^{-(1/2)\delta_S t} + \ldots, \tag{72}$$

with $A_{11}^{(SS)} = (g_2)_{\text{eff}}$ and $\delta_S = E_{S,2} - E_{S,1}$. For the double ratio $R_3(t, t/2)$ we obtain, after Taylor-expanding the square root and omitting terms that decay faster than $e^{-\delta_S t}$ or $e^{-\delta_T t}$,

$$\begin{aligned} R_3(t, t/2) = A_{11}^{(ST)} &- \frac{A_{11}^{(ST)} |Z_{S,2}|^2 e^{-\delta_S t}}{2|Z_{S,1}|^2} - \frac{A_{11}^{(ST)} |Z_{T,2}|^2 e^{-\delta_T t}}{2|Z_{T,1}|^2} + \Re\left[A_{21}^{(ST)} \frac{Z_{S,2}}{Z_{S,1}}\right] e^{-(1/2)\delta_S t} \\ &+ \Re\left[A_{12}^{(ST)} \frac{Z_{T,2}}{Z_{T,1}}\right] e^{-(1/2)\delta_T t} + \Re\left[A_{22}^{(ST)} \frac{Z_{T,2} Z_{S,2}^*}{Z_{T,1} Z_{S,1}^*}\right] e^{-(1/2)(\delta_S + \delta_T) t} + \ldots, \end{aligned} \tag{73}$$

with $A_{11}^{(ST)} = (g_3)_{\text{eff}}$ and $\delta_S = E_{S,2} - E_{S,1}$, $\delta_T = E_{T,2} - E_{T,1}$. The t-dependent terms in the right-hand sides of Eqs. (71)–(73) are the leading excited-state contributions to the extraction of $(g_i)_{\text{eff}}$ from the ratio method.

III. LATTICE ACTIONS AND PARAMETERS

Our calculations are based on gauge field ensembles generated by the RBC/UKQCD collaboration. These ensembles include $2 + 1$ dynamical light-quark flavors, implemented with a domain-wall action [24–26]. The gluons are implemented with the Iwasaki action [33,34], which is known to reduce the residual chiral symmetry breaking of the domain-wall action [35].

The details of the actions used in generating the ensembles can be found in Ref. [32]. Our analysis includes the ensembles of size $24^3 \times 64$ and $32^3 \times 64$, which are described in Ref. [27]. These ensembles have lattice spacings of approximately 0.112 and 0.085 fm, respectively, so that the spatial volume is about $(2.7\ \text{fm})^3$ in both cases.

At the coarse lattice spacing, we used only the ensemble with $am_{u,d}^{(\text{sea})} = 0.005$, which is the lightest available mass. At the fine lattice spacing, we used the ensembles with the lightest two available values of the sea quark mass, $am_{u,d}^{(\text{sea})} = 0.004$ and $am_{u,d}^{(\text{sea})} = 0.006$. The values for the residual quark mass, which is the additive quark-mass renormalization coming from the residual chiral symmetry breaking at finite extent of the fifth dimension L_s, are approximately $am_{\text{res}} = 0.0032$ at the coarse lattice spacing and $am_{\text{res}} = 0.00067$ at the fine lattice spacing. The sea-strange-quark masses are about 10% above the physical value [27], and we assign a 1.5% systematic uncertainty to our final results for the axial couplings to account for this, based on the size of the effect on similar axial-current observables as determined using mass reweighting in Ref. [27].

We calculated light-quark propagators using exactly the same domain-wall action that was used by the RBC/UKQCD collaboration for the sea quarks, with the same domain-wall height of $aM_5 = 1.8$ and extent of the fifth dimension $L_s = 16$. We used propagator sources smeared according to Eq. (48), with $\sigma = 4.35$ and $n_S = 30$. As summarized in Table I, we calculated propagators for valence quark masses $am_{u,d}^{(\text{val})}$ both equal to and lighter than the sea quark masses. The data with $m_{u,d}^{(\text{val})} < m_{u,d}^{(\text{sea})}$ are referred to as "partially quenched". Also shown in Table I, and plotted in Fig. 1, are the corresponding masses of pions composed of the three different possible combinations of valence and sea quarks. The lightest valence-valence pion mass is 227(3) MeV, at the fine lattice spacing.

For the heavy quark, we use a static action of the form given by Eichten and Hill [22], which corresponds to heavy-quark propagators of the form (57). For the temporal gauge links in this action (or, equivalently, the propagators), we use hypercubic (HYP) smeared links [37] with smearing parameters $\alpha_1 = \alpha_2 = \alpha_3 = 0.75$. This leads to an exponential improvement in the signal-to-noise ratio

TABLE I. Parameters of the gauge field ensembles and quark propagators. The lattice-spacing values are from Ref. [36].

$L^3 \times T$	$am_s^{(\mathrm{sea})}$	$am_{u,d}^{(\mathrm{sea})}$	$am_{u,d}^{(\mathrm{val})}$	a (fm)	$m_\pi^{(\mathrm{ss})}$ (MeV)	$m_\pi^{(\mathrm{vs})}$ (MeV)	$m_\pi^{(\mathrm{vv})}$ (MeV)
$24^3 \times 64$	0.04	0.005	0.001	0.1119(17)	336(5)	294(5)	245(4)
$24^3 \times 64$	0.04	0.005	0.002	0.1119(17)	336(5)	304(5)	270(4)
$24^3 \times 64$	0.04	0.005	0.005	0.1119(17)	336(5)	336(5)	336(5)
$32^3 \times 64$	0.03	0.004	0.002	0.0849(12)	295(4)	263(4)	227(3)
$32^3 \times 64$	0.03	0.004	0.004	0.0849(12)	295(4)	295(4)	295(4)
$32^3 \times 64$	0.03	0.006	0.006	0.0848(17)	352(7)	352(7)	352(7)

[23]. The smearing procedure can be iterated n_{HYP} times, leading to a broader smearing and further improvement of the signal-to-noise ratio. We generated data for $n_{\mathrm{HYP}} = 1$, 2, 3, 5, 10. While all of these actions have the same continuum limit, the dependence of the results on the lattice spacing is expected to be different for different values of n_{HYP}. One may naively expect large discretization effects for large values of n_{HYP}, which correspond to a large spatial extent of the heavy-quark-gluon interaction vertex. We will discuss this in detail when giving the numerical results in Sec. IV. Our final axial coupling results only make use of data generated with $n_{\mathrm{HYP}} = 1$, 2, 3.

As mentioned in Sec. II C, to perform the contractions for the three-point functions (53), we required pairs of light-quark propagators with sources located at the same spatial point and separated by t/a steps in the time direction. The numbers of measurements (propagator pairs) for each value of t/a are given in Table II. At the coarse lattice spacing, our data come from typically 120 statistically independent gauge field configurations; at the fine lattice spacing we used about 240 statistically independent gauge configurations of the $am_{u,d}^{(\mathrm{sea})} = 0.004$ ensemble and 180 for the $am_{u,d}^{(\mathrm{sea})} = 0.006$ ensemble. In most cases, we have more measurements than configurations, because we generated propagators from multiple source points on the lattice. In those cases, we have averaged over the source locations before the further analysis to remove possible autocorrelations.

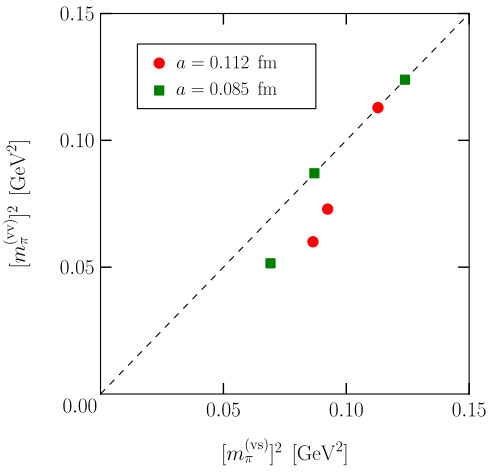

FIG. 1 (color online). The values of $[m_\pi^{(\mathrm{vv})}]^2$ and $[m_\pi^{(\mathrm{vs})}]^2$ used in our calculation. The dashed line indicates the unquenched case $m_\pi^{(\mathrm{vv})} = m_\pi^{(\mathrm{vs})}$.

Within each of the three gauge field ensembles that we used, the data from different source-sink separations, different valence quark masses, and different values of n_{HYP} are correlated with each other. In our analysis, we properly took into account these correlations using the statistical bootstrap procedure. The initial averaging over source locations mentioned above was also required to reduce all data from the same ensemble to matching ordered sets of measurements, as necessary to calculate the covariance matrices. It turned out that the correlations between the $am_{u,d}^{(\mathrm{val})} = 0.001$ and $am_{u,d}^{(\mathrm{val})} = 0.002/0.005$ data at the coarse lattice spacing were very weak even though the data came from the same ensemble of gauge field configurations. The reason was that all source locations used for the $am_{u,d}^{(\mathrm{val})} = 0.001$ propagators were distinct from those used at $am_{u,d}^{(\mathrm{val})} = 0.002/0.005$. In contrast, the data from $am_{u,d}^{(\mathrm{val})} = 0.002$ and $am_{u,d}^{(\mathrm{val})} = 0.005$ came from almost identical source locations, resulting in very strong correlations (these correlations were advantageous in constraining

TABLE II. Number of propagator pairs used for the three-point functions for various values of the source-sink separation t/a.

$L^3 \times T$	$am_{u,d}^{(\mathrm{val})}$	t/a	N_{meas} (approx.)
$24^3 \times 64$	0.001	10	550
$24^3 \times 64$	0.001	9, 8, 7, 6	240
$24^3 \times 64$	0.001	5	460
$24^3 \times 64$	0.001	4	120
$24^3 \times 64$	0.002	10	880
$24^3 \times 64$	0.002	9, 8, 7, 6, 4	240
$24^3 \times 64$	0.002	5	480
$24^3 \times 64$	0.005	10	960
$24^3 \times 64$	0.005	9, 8, 7, 6, 4	240
$24^3 \times 64$	0.005	5	480
$32^3 \times 64$	0.002	12	1200
$32^3 \times 64$	0.002	9, 6	480
$32^3 \times 64$	0.004	12	1200
$32^3 \times 64$	0.004	9, 6	480
$32^3 \times 64$	0.006	13	700

the quark-mass dependence in our chiral fits). Similarly, at the fine lattice spacing, the data from $am_{u,d}^{(\mathrm{val})} = 0.002$ and $am_{u,d}^{(\mathrm{val})} = 0.004$ came from identical source locations, leading to strong correlations.

For the axial-current renormalization parameter, we use the values obtained nonperturbatively by the RBC/UKQCD collaboration, which are [27]

$$Z_A = \begin{cases} 0.7019(26) & \text{for } a = 0.112 \text{ fm}, \\ 0.7396(17) & \text{for } a = 0.085 \text{ fm}. \end{cases} \quad (74)$$

IV. DATA ANALYSIS

A. Ratios

Examples of numerical results for the ratios (63)–(65) are shown in Fig. 2 (for $a = 0.112$ fm) and Fig. 3 (for $a = 0.085$ fm). These ratios were calculated using statistical bootstrap to take into account the strong correlations between the three-point and two-point functions in numerator and denominator. Because of these correlations, the statistical uncertainties in the ratios are found to be smaller than those in the three-point functions themselves. To maximize correlations, it is essential to use the two-point functions from the source locations matching those of the three-point functions. The figures show results at two different values of the source-sink separation t in each case, for $am_{u,d}^{(\mathrm{val})} = 0.002$ and $n_{\mathrm{HYP}} = 3$.

We observe clear plateaus of $R_i(t, t')$ as a function of t', whose extent appears to be slightly larger for the simple ratios R_1 and R_2 compared to the double ratio R_3. The plateaus in t' indicate that in these regions contributions from off-diagonal matrix elements of the axial current between a ground-state hadron and an excited state are negligible in comparison to the statistical uncertainties, because such a transition matrix element would introduce t' dependence [see Eqs. (68) and (69)]. For R_1, the flatness with respect to t' has previously been observed and discussed in Refs. [15,18].

We averaged $R_i(t, t')$ over a symmetric range of t' values around $t/2$ in a region where there was no statistically significant t' dependence (requiring that the χ^2/d.o.f. of correlated constant fits be of order 1). These regions and the extracted values, which we denote as $R_i(t)$, are indicated in Figs. 2 and 3 for representative data sets. The averaging in the plateau region is essentially equivalent to using

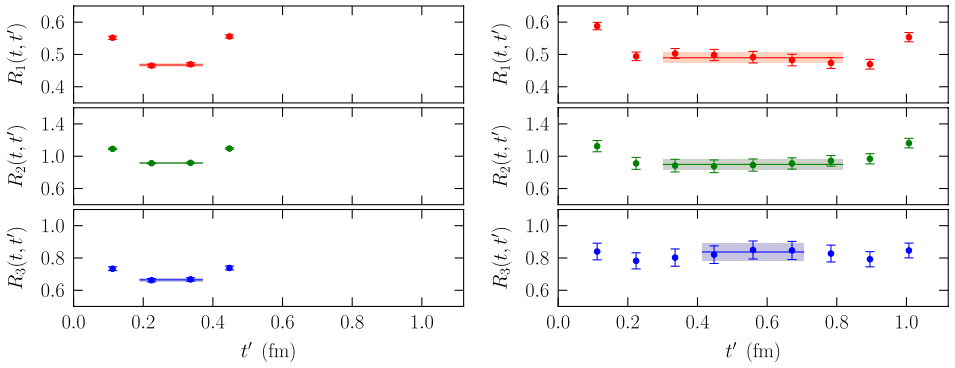

FIG. 2 (color online). Ratios R_1, R_2, R_3 as a function of the current insertion time slice t', for the source-sink separations $t/a = 5$ (left) and $t/a = 10$ (right). The data shown are for $a = 0.112$ fm, $n_{\mathrm{HYP}} = 3$, and $am_{u,d}^{(\mathrm{val})} = 0.002$.

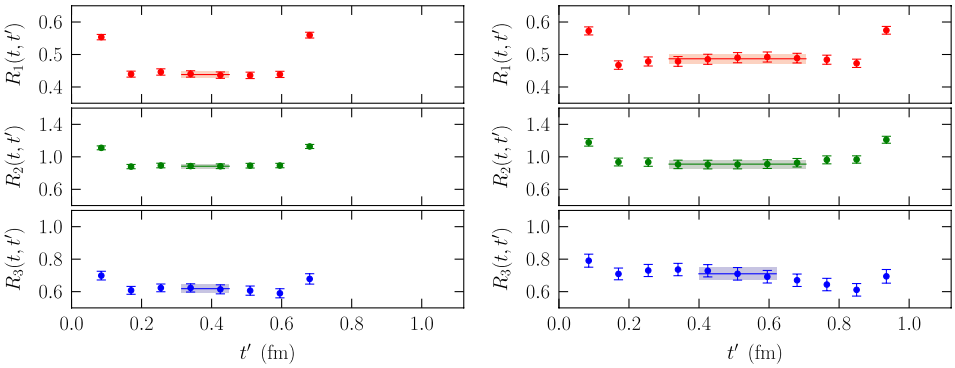

FIG. 3 (color online). Ratios R_1, R_2, R_3 as a function of the current insertion time slice t', for the source-sink separations $t/a = 9$ (left) and $t/a = 12$ (right). The data shown here are for $a = 0.085$ fm and $n_{\mathrm{HYP}} = 3$, and $am_{u,d}^{(\mathrm{val})} = 0.002$.

$$R_i(t, t/2). \tag{75}$$

Indeed, because of the strong corrrelation between neighboring t' points, we found that the averaging over t' in the plateau region (which is again performed using bootstrap) gives almost the same result and uncertainty as $R_i(t, t/2)$. An alternative method for defining $R_i(t)$ is discussed in Appendix B.

Summary plots of all the extracted values for $R_1(t)$, $R_2(t)$, and $R_3(t)$ at the different quark masses, lattice spacings, and numbers of heavy-quark smearing iterations n_{HYP} are given in Appendix A. Note that the numbers of measurements vary (see Table II). The statistical uncertainties are found to grow quickly when t is increased or $am_{u,d}^{(\mathrm{val})}$ is decreased, as expected [38]. Furthermore, the statistical uncertainties are reduced with every iteration of HYP smearing in the static heavy-quark action, which is also expected [23]. While the results for $(g_i)_{\mathrm{eff}} = \lim_{t\to\infty} R_i(t)$ from all fixed values of n_{HYP} will become equal when the lattice spacing is taken to zero, at nonzero lattice spacing different values of n_{HYP} will have different discretization errors. Indeed, R_1 and R_2 are seen to increase with n_{HYP}. Remarkably, the results for R_3 are almost independent of n_{HYP} within the statistical uncertainties even at nonzero lattice spacing. See also Sec. IV B for the n_{HYP} dependence of $(g_i)_{\mathrm{eff}} = \lim_{t\to\infty} R_i(t)$.

B. Extrapolation to infinite source-sink separation

The effective axial couplings $(g_i)_{\mathrm{eff}}$ at given values of the lattice spacing, the quark masses, and n_{HYP}, are defined as the infinite-time limits of $R_i(t)$:

$$(g_i)_{\mathrm{eff}} = \lim_{t\to\infty} R_i(t). \tag{76}$$

The t dependence of $R_i(t)$ is caused by excited states, and at sufficiently large t, the contributions from the first relevant excitation dominates. The expected functional form of $R_1(t)$, $R_2(t)$, and $R_3(t)$ in this regime is shown in Eqs. (71)–(73), respectively. As can be seen in these equations, the "diagonal" contributions proportional to the matrix elements A_{11} and A_{22} decay exponentially like

$$e^{-\delta t}, \tag{77}$$

where δ is the energy gap to the first excited state that has a nonzero overlap with the corresponding interpolating field as defined in Eq. (47); $\delta = \delta_P$ for R_1, $\delta = \delta_S$ for R_2, and $\delta = \min(\delta_S, \delta_T)$ for R_3. Additionally, there are "off-diagonal" contributions proportional to the matrix elements A_{12} and A_{21}, which decay only like

$$e^{-(1/2)\delta t}. \tag{78}$$

However, as discussed in Sec. IV A and Ref. [18], these off-diagonal contributions appear to be small, because the numerical results for $R(t, t')$ show plateaus as a function of t'.

We performed correlated fits to the lattice data for $R_i(t, a, m, n_{\mathrm{HYP}})$, which depends on the source-sink separation t, the lattice spacing a, the quark masses (here denoted generically as m), and n_{HYP}, using the following functions:

$$\begin{aligned}
R_1(t, a, m, n_{\mathrm{HYP}}) &= (g_1)_{\mathrm{eff}}(a, m, n_{\mathrm{HYP}}) \\
&\quad - A_1(a, m, n_{\mathrm{HYP}}) e^{-\delta_1(a,m,n_{\mathrm{HYP}})t}, \\
R_2(t, a, m, n_{\mathrm{HYP}}) &= (g_2)_{\mathrm{eff}}(a, m, n_{\mathrm{HYP}}) \\
&\quad - A_2(a, m, n_{\mathrm{HYP}}) e^{-\delta_2(a,m,n_{\mathrm{HYP}})t}, \\
R_3(t, a, m, n_{\mathrm{HYP}}) &= (g_3)_{\mathrm{eff}}(a, m, n_{\mathrm{HYP}}) \\
&\quad - A_3(a, m, n_{\mathrm{HYP}}) e^{-\delta_3(a,m,n_{\mathrm{HYP}})t}.
\end{aligned} \tag{79}$$

Here δ_i is the energy gap to the dominant excitation in R_i. Because δ_i is not constrained, it does not matter whether or not we include a factor of $1/2$ in the exponent. Since the energy gap δ_i is positive by definition, we choose to parametrize it as

$$a\delta_i(a, m, n_{\mathrm{HYP}}) = e^{l_i(a,m,n_{\mathrm{HYP}})}, \tag{80}$$

using the logarithm $l_i(a, m, n_{\mathrm{HYP}})$ as the fit parameter.

Because the statistical uncertainties in R_i grow exponentially as t is increased, we were only able to perform the lattice QCD calculations in the range $t \lesssim 1.1$ fm. As can be seen in Table II, at the coarse lattice spacing ($a = 0.112$ fm) we have data for $t/a = 4, 5, 6, 7, 8, 9, 10$. We found that the functions (79) described the data from the coarse lattice spacing well for all these values of t/a. The smallest statistical uncertainties are obtained for $am_{u,d}^{(\mathrm{val})} = 0.005$ and $n_{\mathrm{HYP}} = 10$, and therefore we first performed unconstrained fits to this data set, obtaining the following fit results (l_i converted to $\delta_i = e^{l_i}/a$):

$$\begin{aligned}
&(g_1)_{\mathrm{eff}} = 0.5264 \pm 0.0090, && A_1 = 0.53 \pm 0.39, \\
&\delta_1 = (1.08 \pm 0.38)\ \mathrm{GeV}, && \chi^2/\mathrm{d.o.f.} = 1.07, \\
&(g_2)_{\mathrm{eff}} = 1.037 \pm 0.033, && A_2 = 0.73 \pm 0.35, \\
&\delta_2 = (0.75 \pm 0.29)\ \mathrm{GeV}, && \chi^2/\mathrm{d.o.f.} = 0.31, \\
&(g_3)_{\mathrm{eff}} = 0.827 \pm 0.032, && A_3 = 0.98 \pm 0.25, \\
&\delta_3 = (0.66 \pm 0.16)\ \mathrm{GeV}, && \chi^2/\mathrm{d.o.f.} = 0.41.
\end{aligned} \tag{81}$$

The corresponding fits and the data points are shown in the left-hand side of Fig. 4. Notice that the fit to R_1 gives an energy gap consistent with recent lattice QCD results for the $2S$ radial excitation energy of about 0.75 GeV [39,40]. This is expected, because our interpolating fields (47) for the heavy-light mesons have S-wave-type smearing and therefore do not couple to the lower-lying $1P$ state. The fit result (and the flatness of the plateau as a function of t') indicates that the data for R_1 are dominated by

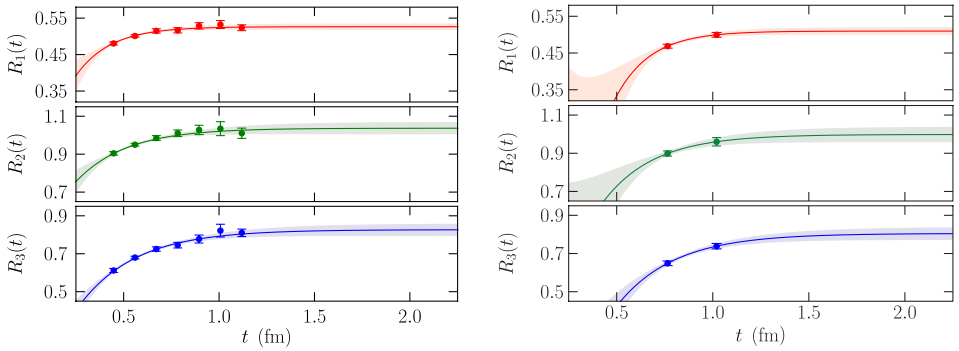

FIG. 4 (color online). Fits of the t dependence of $R_1(t)$, $R_2(t)$, $R_3(t)$, for $n_{\mathrm{HYP}} = 10$, using the functions defined in Eq. (79). The left-hand side shows unconstrained fits of the $a = 0.112$ fm, $am_{u,d}^{(\mathrm{val})} = 0.005$ data; the right-hand side shows fits of the $a = 0.085$ fm, $am_{u,d}^{(\mathrm{val})} = 0.004$ data, where the energy gap was constrained using information from (81).

$$R_1(t) \approx (g_1)_{\mathrm{eff}} + \left|\frac{Z_{P(2S)}}{Z_{P(1S)}}\right|^2 (A_{2S,2S}^{(PP^*)} - A_{1S,1S}^{(PP^*)}) e^{-\delta_P t}, \quad (82)$$

with a negligible off-diagonal matrix element $A_{2S,1S}^{(PP^*)} \approx 0$.

At the fine lattice spacing, we only have data for $t/a = 6, 9, 12$ (for $am_{u,d}^{(\mathrm{val})} = 0.002, 0.004$) or $t/a = 13$ (for $am_{u,d}^{(\mathrm{val})} = 0.006$). Because the energy gap in physical units is not expected to have an a dependence that is larger than the statistical uncertainties in (81), it is possible to use the fit results for l_i from the coarse lattice spacing to constrain the parameters l_i at the fine lattice spacing (at similar pion masses). As a first step, we performed fits to the data from the fine lattice spacing with $am_{u,d}^{(\mathrm{val})} = 0.004$ and $n_{\mathrm{HYP}} = 10$, where only the parameters l_i were constrained using an augmented χ^2 with a Gaussian prior for l_i,

$$\chi^2 \to \chi^2 + \frac{(l_i - \tilde{l}_i)^2}{\tilde{\sigma}_{l_i}^2}. \quad (83)$$

Here, $\tilde{l}_i$ and $\tilde{\sigma}_{l_i}$ are the central values and uncertainties of the (scaled) energy gap parameters from the fit to the coarse $am_{u,d}^{(\mathrm{val})} = 0.005$, $n_{\mathrm{HYP}} = 10$ data, Eq. (81). The fits to the data from the fine lattice spacing with $am_{u,d}^{(\mathrm{val})} = 0.004$ and $n_{\mathrm{HYP}} = 10$ then gave

$$\begin{aligned}
(g_1)_{\mathrm{eff}} &= 0.510 \pm 0.011, \qquad A_1 = 2.7 \pm 3.6, \\
\delta_1 &= (1.08 \pm 0.38)\ \mathrm{GeV}, \qquad (g_2)_{\mathrm{eff}} = 0.998 \pm 0.041, \\
A_2 &= 1.8 \pm 1.7, \qquad \delta_2 = (0.75 \pm 0.29)\ \mathrm{GeV}, \\
(g_3)_{\mathrm{eff}} &= 0.805 \pm 0.034, \qquad A_3 = 2.0 \pm 1.0, \\
\delta_3 &= (0.66 \pm 0.16)\ \mathrm{GeV}. \quad (84)
\end{aligned}$$

At the fine lattice spacing, it was necessary to remove the data points with the shortest separation $t/a = 6$ to obtain acceptable single-exponential fits. Therefore, the resulting gap parameter matches exactly the prior, and $\chi^2/\mathrm{d.o.f.}$ is undefined. The central values of the overlap parameters A_i in (84) are larger than in (81), indicating a stronger overlap of the interpolating fields with excited states at the fine lattice spacing. Different overlap factors were expected here, because the smearing width of the light-quark fields in physical units was different (we used the same smearing width in lattice units for both lattice spacings). The fit curves are shown in the right-hand side of Fig. 4.

We then performed new fits to the data for all values of the quark masses and n_{HYP}. For those fits, the parameters $(g_i)_{\mathrm{eff}}(a, m, n_{\mathrm{HYP}})$ were left unconstrained, but Gaussian priors were used for both l_i and A_i, with central values and widths as taken from the initial fits (81) for the coarse lattice spacing and (84) for the fine lattice spacing. Examples of these fits are shown in Fig. 5. The only assumption made by using the priors is that the dependence of l_i and A_i on n_{HYP} and on the quark masses is smaller than the width of the priors as determined by the statistical uncertainties in (81) and (84). Given that these widths were 25% or larger in all cases, this appears to be a reasonable assumption. As a test, we also performed unconstrained fits where possible, which gave consistent results but were less stable. The results for $(g_i)_{\mathrm{eff}}(a, m, n_{\mathrm{HYP}})$ are given in Tables III and IV, and plotted in Fig. 6. The central values and uncertainties shown there are bootstrap averages and 68% widths, respectively, from repeated correlated fits of the t dependence for a bootstrap ensemble of data.

To estimate the systematic uncertainties caused by higher excited states, we calculated the shifts in $(g_i)_{\mathrm{eff}}$ for a representative data set at the coarse lattice spacing ($am_{u,d}^{(\mathrm{val})} = 0.002$, $n_{\mathrm{HYP}} = 3$) when removing one or two data points with the smallest t/a ($= 4, 5$) from the fits, or adding a second exponential to the fit function,

$$R_i(t) = (g_i)_{\mathrm{eff}} - A_i e^{-\delta_i t} - B_i A_i e^{-(\delta_i + \delta_i^{(2)})t}. \quad (85)$$

Because the available data were not sufficient to determine the new parameters B_i and $\delta_i^{(2)}$, we used Gaussian priors to constrain these parameters to physically reasonable values. The parameters B_i describe the amplitudes of the second-excited-state contribution, relative to the first-excited-state contribution, and we set $\tilde{B}_i = 0$, $\tilde{\sigma}_{B_i} = 2$. For the energy

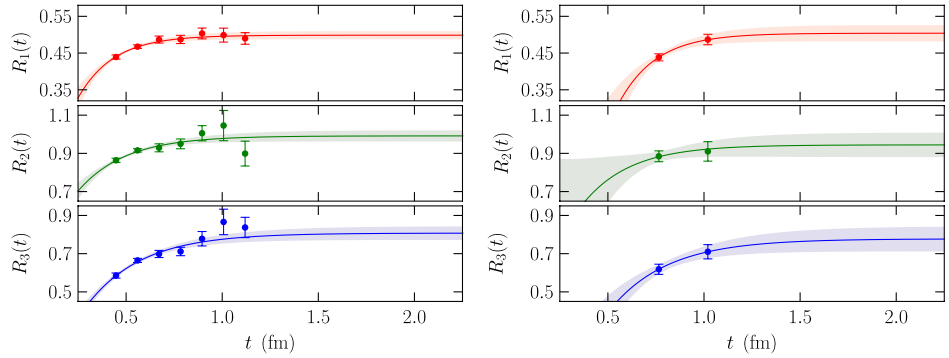

FIG. 5 (color online). Fits of the t dependence of $R_1(t)$, $R_2(t)$, $R_3(t)$, for $n_{\rm HYP} = 3$, using the functions defined in Eq. (79). The left-hand side shows the $a = 0.112$ fm, $am_{u,d}^{(\rm val)} = 0.002$ data, and the right-hand side shows the $a = 0.085$ fm, $am_{u,d}^{(\rm val)} = 0.002$ data. In both cases, the overlap parameters A_i and energy gaps δ_i were constrained using information from (81) and (84).

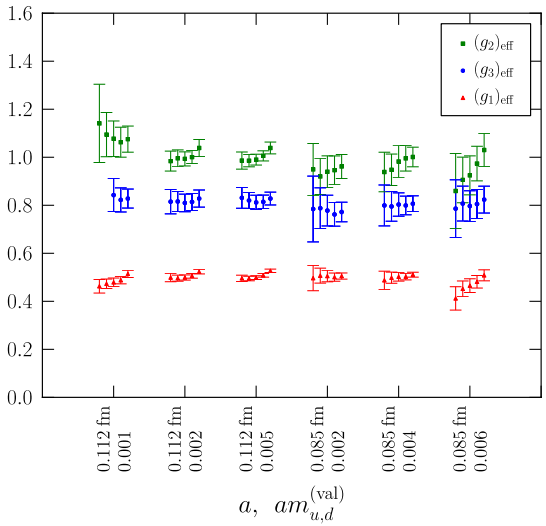

FIG. 6 (color online). Plot of the results for $(g_i)_{\rm eff}$ from Tables III and IV. For each combination of a and $am_{u,d}^{(\rm val)}$, results from up to five different values of $n_{\rm HYP}$ are shown (from left to right: $n_{\rm HYP} = 1, 2, 3, 5, 10$; points offset horizontally for legibility).

gaps $a\delta_i^{(2)} = e^{l_i^{(2)}}$ we used priors with central values equal to 2/3 times the fit results for δ_i in (81), and widths of 100%. The fitted parameters $(g_i)_{\rm eff}$ and the corresponding shifts $\delta(g_i)_{\rm eff}$ for the different cases are shown in Table V. Since the shifts $\delta(g_i)_{\rm eff}$ themselves have statistical uncertainties $\sigma\delta(g_i)_{\rm eff}$, we choose to quote the maximum value of

$$\sqrt{[\delta(g_i)_{\rm eff}]^2 + [\sigma\delta(g_i)_{\rm eff}]^2} \tag{86}$$

from the three different methods (removing $t/a = 4$, removing $t/a = 4, 5$, or adding a second exponential) as our estimate of the systematic uncertainties in $(g_i)_{\rm eff}$ caused by higher excited states. The final estimates are 1.7%, 2.8%, and 4.9% for g_1, g_2, and g_3, respectively.

Because the shifts $\delta(g_i)_{\rm eff}$ in Table V are consistent with zero in most cases, an alternative way of estimating the systematics is to consider only the increase (calculated with quadrature) in the *uncertainties* of the fitted parameters when the fits are modified by removing data points or including higher-order terms. We will use that method for the chiral fits at the end of Sec. IV C, see Eq. (96). The two different methods (86) and (96) for calculating the size of the systematic uncertainties give consistent values.

C. Extraction of the axial couplings g_1, g_2, and g_3 using HHχPT fits of the data

In the previous section, we obtained results for the effective axial couplings $(g_i)_{\rm eff}(a, m, n_{\rm HYP})$ at two different lattice spacings a, multiple values for the quark masses $am_{u,d}^{(\rm sea)}$ and $am_{u,d}^{(\rm val)}$, and multiple values for the heavy-quark gauge-link smearing parameter $n_{\rm HYP}$ (corresponding to multiple heavy-quark lattice discretizations). All data are for a finite spatial volume of about $(2.7\ \text{fm})^3$. In the following, we discuss how we extracted the axial couplings g_1, g_2, g_3, which are the parameters of the continuum heavy-hadron chiral perturbation theory Lagrangian (8), from the data for $(g_i)_{\rm eff}(a, m, n_{\rm HYP})$.

To fit the quark-mass and volume dependence of $(g_i)_{\rm eff}$ we use the next-to-leading-order predictions from HHχPT [20], which were already shown in Eq. (46). Here, we extend these formulas to include the leading effects of the nonzero lattice spacing a. These leading effects are quadratic in a, with coefficients $d_{i,n_{\rm HYP}}$ that depend on $n_{\rm HYP}$. We do not expect $O(a)$ errors because of the chiral symmetry of the domain-wall action used for the light quarks (neglecting the small effects caused by the residual chiral symmetry breaking at finite L_s [27]) and the automatic $O(a)$ improvement of the static heavy-quark action. Higher-order effects in the a- and m_π dependence of $(g_i)_{\rm eff}$ are discussed at the end of this section.

For $(g_1)_{\rm eff}$, the fit function is given by

$$(g_1)_{\rm eff}(a,m,n_{\rm HYP}) = g_1\Big[1 - \frac{2}{f^2}\mathcal{I}(m_\pi^{(\rm vs)}) + \frac{g_1^2}{f^2}\{4\mathcal{H}(m_\pi^{(\rm vs)},0) - 4\delta_{VS}^2\mathcal{H}_{\eta'}(m_\pi^{(\rm vv)},0)\} + c_1^{(\rm vv)}[m_\pi^{(\rm vv)}]^2 + c_1^{(\rm vs)}[m_\pi^{(\rm vs)}]^2 + d_{1,n_{\rm HYP}}a^2\Big]. \quad (87)$$

Similarly, for $(g_2)_{\rm eff}$ and $(g_3)_{\rm eff}$, we use

$$(g_2)_{\rm eff}(a,m,n_{\rm HYP}) = g_2\Big[1 - \frac{2}{f^2}\mathcal{I}(m_\pi^{(\rm vs)}) + \frac{g_2^2}{f^2}\Big\{\frac{3}{2}\mathcal{H}(m_\pi^{(\rm vs)},0) - \delta_{VS}^2\mathcal{H}_{\eta'}(m_\pi^{(\rm vv)},0)\Big\} + \frac{g_3^2}{f^2}\{2\mathcal{H}(m_\pi^{(\rm vs)},-\Delta) - \mathcal{H}(m_\pi^{(\rm vv)},-\Delta) - 2\mathcal{K}(m_\pi^{(\rm vs)},-\Delta,0)\} + c_2^{(\rm vv)}[m_\pi^{(\rm vv)}]^2 + c_2^{(\rm vs)}[m_\pi^{(\rm vs)}]^2 + d_{2,n_{\rm HYP}}a^2\Big], \quad (88)$$

$$(g_3)_{\rm eff}(a,m,n_{\rm HYP}) = g_3\Big[1 - \frac{2}{f^2}\mathcal{I}(m_\pi^{(\rm vs)}) + \frac{g_3^2}{f^2}\Big\{\mathcal{H}(m_\pi^{(\rm vs)},-\Delta) - \frac{1}{2}\mathcal{H}(m_\pi^{(\rm vv)},-\Delta) + \frac{3}{2}\mathcal{H}(m_\pi^{(\rm vv)},\Delta) + 3\mathcal{H}(m_\pi^{(\rm vs)},\Delta) - \mathcal{K}(m_\pi^{(\rm vs)},\Delta,0)\Big\} + \frac{g_2^2}{f^2}\{-\mathcal{H}(m_\pi^{(\rm vs)},\Delta) - \mathcal{H}(m_\pi^{(\rm vv)},\Delta) + \mathcal{H}(m_\pi^{(\rm vs)},0) - \delta_{VS}^2\mathcal{H}_{\eta'}(m_\pi^{(\rm vv)},0)\} + c_3^{(\rm vv)}[m_\pi^{(\rm vv)}]^2 + c_3^{(\rm vs)}[m_\pi^{(\rm vs)}]^2 + d_{3,n_{\rm HYP}}a^2\Big]. \quad (89)$$

The functions $\mathcal{I}$, $\mathcal{H}$, $\mathcal{H}_{\eta'}$ and $\mathcal{K}$ are the chiral loop corrections [20]. They include finite-volume effects and therefore they also depend on the lattice size. Furthermore, these functions depend on the renormalization scale μ, but this scale dependence is absorbed by the fit parameters $c_i^{(\rm vv)}$ and $c_i^{(\rm vs)}$, as we checked explicitly by varying μ in the fits. We set the pion decay constant to $f = 132$ MeV and the S-T mass splitting in Eqs. (88) and (89) to $\Delta = 200$ MeV. This value of Δ is consistent with experiments [13,29] and with our lattice data (we also checked that varying Δ within a few percent does not significantly affect the results for the axial couplings). We calculated the covariances of all correlated data points in Tables III and IV using bootstrap, and performed fully correlated fits using the inverse of the covariance matrix in the definition of χ^2. This method propagates the uncertainties and correlations of $(g_i)_{\rm eff}$, as obtained from the fits to the ratios R_i, into the extracted parameters g_i of the HHχPT Lagrangian.

Results from fits of the $(g_1)_{\rm eff}$ data using the function (87) are given in Table VI and Fig. 7. The fit parameters are g_1, $c_1^{(\rm vv)}$, $c_1^{(\rm vs)}$, and $\{d_{1,n_{\rm HYP}}\}$ (the latter for all values of $n_{\rm HYP}$ that were included in the fit). We performed fits that

TABLE III. Effective axial couplings $(g_i)_{\rm eff}$ at $a = 0.112$ fm, obtained by extrapolating $R_i(t)$ to $t = \infty$. At $am_{u,d}^{(\rm val)} = 0.001$ we do not have results for $n_{\rm HYP} = 1, 2$, because the statistical fluctuations were too large to calculate the square root of the double ratio, Eq. (65).

$am_{u,d}^{(\rm sea)}$	$am_{u,d}^{(\rm val)}$	$n_{\rm HYP}$	$(g_1)_{\rm eff}$	$(g_2)_{\rm eff}$	$(g_3)_{\rm eff}$
0.005	0.001	1	0.463(28)	1.14(16)	...
0.005	0.001	2	0.473(20)	1.094(92)	...
0.005	0.001	3	0.479(18)	1.077(74)	0.843(68)
0.005	0.001	5	0.488(15)	1.063(62)	0.822(50)
0.005	0.001	10	0.514(15)	1.075(54)	0.828(40)
0.005	0.002	1	0.499(17)	0.984(42)	0.815(51)
0.005	0.002	2	0.496(13)	0.996(35)	0.816(41)
0.005	0.002	3	0.499(11)	0.993(29)	0.810(37)
0.005	0.002	5	0.5059(96)	1.001(27)	0.814(35)
0.005	0.002	10	0.5230(89)	1.039(35)	0.828(36)
0.005	0.005	1	0.496(13)	0.986(36)	0.831(43)
0.005	0.005	2	0.4950(94)	0.986(25)	0.820(34)
0.005	0.005	3	0.4987(80)	0.990(23)	0.812(30)
0.005	0.005	5	0.5080(74)	1.006(21)	0.814(28)
0.005	0.005	10	0.5270(71)	1.039(25)	0.828(27)

TABLE IV. Effective axial couplings $(g_i)_{\text{eff}}$ at $a = 0.085$ fm, obtained by extrapolating $R_i(t)$ to $t = \infty$.

$am_{u,d}^{(\text{sea})}$	$am_{u,d}^{(\text{val})}$	n_{HYP}	$(g_1)_{\text{eff}}$	$(g_2)_{\text{eff}}$	$(g_3)_{\text{eff}}$
0.004	0.002	1	0.496(52)	0.95(11)	0.78(14)
0.004	0.002	2	0.507(31)	0.920(75)	0.788(85)
0.004	0.002	3	0.505(24)	0.940(66)	0.778(64)
0.004	0.002	5	0.501(17)	0.946(59)	0.762(49)
0.004	0.002	10	0.505(13)	0.962(50)	0.772(41)
0.004	0.004	1	0.488(38)	0.939(82)	0.799(85)
0.004	0.004	2	0.498(23)	0.948(65)	0.795(62)
0.004	0.004	3	0.502(18)	0.982(66)	0.803(49)
0.004	0.004	5	0.503(14)	0.995(53)	0.799(39)
0.004	0.004	10	0.511(10)	1.001(41)	0.807(33)
0.006	0.006	1	0.412(49)	0.86(16)	0.79(12)
0.006	0.006	2	0.452(33)	0.905(95)	0.807(73)
0.006	0.006	3	0.465(29)	0.925(81)	0.797(64)
0.006	0.006	5	0.481(26)	0.974(72)	0.805(60)
0.006	0.006	10	0.508(23)	1.030(68)	0.824(56)

included data with multiple values of n_{HYP}, as well as individual fits including only data with one value of n_{HYP}. The fits that included multiple values of n_{HYP} enforced a common continuum limit of the data with different n_{HYP}, but with separate a^2-coefficients $d_{1,n_{\text{HYP}}}$ for each n_{HYP}. While we know that the actual continuum limit for all values of n_{HYP} has to be the same (if we took a to zero in the numerical calculations), we only have data for two different values of a, and one may question whether the approach of the continuum limit is described by a simple a^2 dependence as assumed in Eq. (87). In particular, one may be worried that large values of n_{HYP}, which correspond to more spatially extended heavy-quark actions, could lead to non-negligible contributions from higher powers of a [23]. To investigate this, we started from a fit that included all values of n_{HYP} (1, 2, 3, 5, 10), and then successively removed the data with the largest values of n_{HYP}. As can be seen in Table VI and Fig. 7, the fit including the data from all values of n_{HYP} had a poor quality, $Q = 0.17$, and gave a somewhat low value for g_1. After excluding $n_{\text{HYP}} = 10$ and $n_{\text{HYP}} = 5$, the fits had a good quality and the results for g_1 were stable under further exclusions of the largest n_{HYP} values. The fit including $n_{\text{HYP}} = 1, 2, 3$, which has $Q = 0.70$, gave the result

$$g_1 = 0.449 \pm 0.047_{\text{stat}}. \tag{90}$$

Estimates of the systematic uncertainties in (90) will be given at the end of this section. The results from the fits including only one value of n_{HYP} were all consistent with (90), even for $n_{\text{HYP}} = 10$. This suggests that higher powers of a^2 are actually negligible for the values of the lattice spacings considered here ($a = 0.085$ fm and $a = 0.112$ fm). The deviating value of g_1 as well as the poor Q for the fit that included all values of n_{HYP} simultaneously are likely caused by technical issues with the covariance-fitting of highly correlated data, associated with small eigenvalues of the data correlation matrix [41]. We will return to the discussion of higher-order discretization effects at the end of this section.

For the baryonic axial couplings, we performed simultaneous, fully correlated fits to the data for $(g_2)_{\text{eff}}$ and $(g_3)_{\text{eff}}$ using the functions (88) and (89), with the fit parameters g_2, g_3, $c_2^{(\text{vv})}$, $c_3^{(\text{vv})}$, $c_2^{(\text{vs})}$, $c_3^{(\text{vs})}$ and $\{d_{2,n_{\text{HYP}}}, d_{3,n_{\text{HYP}}}\}$ (the latter for all values of n_{HYP} that were included in the fit). As already discussed in the fits for $(g_1)_{\text{eff}}$, we performed fits that included data with multiple values of n_{HYP}, as well as individual fits including only data with one value of n_{HYP}. The results are shown in Table VII and Fig. 8. Again, we select the fit that includes $n_{\text{HYP}} = 1, 2, 3$, which gives

TABLE V. Fits used to estimate systematic uncertainties from higher excited states. Data for $a = 0.112$ fm, $am_{u,d}^{(\text{val})} = 0.002$, $n_{\text{HYP}} = 3$. Shown are the fit results for $(g_i)_{\text{eff}}$, as well as the differences $\delta(g_i)_{\text{eff}}$ to the original fit result, calculated using bootstrap.

Fit	$(g_1)_{\text{eff}}$	$\delta(g_1)_{\text{eff}}$	$(g_2)_{\text{eff}}$	$\delta(g_2)_{\text{eff}}$	$(g_3)_{\text{eff}}$	$\delta(g_3)_{\text{eff}}$
Original	0.499(11)	0	0.993(29)	0	0.810(36)	0
$t/a = 4$ removed	0.496(13)	0.0030(76)	0.975(35)	0.016(19)	0.783(43)	0.026(15)
$t/a = 4, 5$ removed	0.494(12)	0.0041(76)	0.984(41)	0.009(26)	0.807(54)	0.003(30)
Second exponential added	0.498(11)	0.0009(77)	0.988(30)	0.005(21)	0.796(40)	0.014(36)

TABLE VI. Results for the mesonic axial coupling g_1, obtained by fitting the data for $(g_1)_{\rm eff}$ using the function (87). The first four rows show the results from fits which include data with multiple values of the heavy-quark smearing parameter $n_{\rm HYP}$. The remaining rows show the results from fits with only one value of $n_{\rm HYP}$. The number of degrees of freedom (d.o.f.) is given in the form (number of data points)—(number of fit parameters). The last column of the table gives the quality of the fit $Q = \Gamma(\text{d.o.f.}/2, \chi^2/2)$.

$n_{\rm HYP}$	g_1	d.o.f.	χ^2/d.o.f.	Q
1, 2, 3, 5, 10	0.371(28)	30 − 8	1.3	0.17
1, 2, 3, 5	0.401(39)	24 − 7	1.2	0.29
1, 2, 3	0.449(47)	18 − 6	0.75	0.70
1, 2	0.440(60)	12 − 5	0.85	0.54
10	0.450(38)	6 − 4	0.09	0.91
5	0.468(47)	6 − 4	0.61	0.55
3	0.482(55)	6 − 4	0.73	0.49
2	0.465(66)	6 − 4	1.0	0.36
1	0.49(10)	6 − 4	0.72	0.49

$$g_2 = 0.84 \pm 0.20_{\rm stat}, \qquad g_3 = 0.71 \pm 0.12_{\rm stat}. \tag{91}$$

This fit also had the highest value of the quality of fit, $Q = 0.92$. Estimates of the systematic uncertainties in (91) will be given at the end of this section. As can be seen in Fig. 8, the results (91) are in fact consistent with the results from all other fits within the statistical uncertainties, demonstrating that heavy-quark discretization errors are under good control. The covariance matrix for g_2 and g_3 is

$$\text{Cov} = \begin{pmatrix} 0.040 & 0.011 \\ 0.011 & 0.014 \end{pmatrix}. \tag{92}$$

The corresponding likelihood function is plotted in Fig. 9.

As another check, we performed fits of $(g_i)_{\rm eff}$ where we excluded all the partially quenched data (i.e keeping only the unitary data with $m_\pi^{(\rm vv)} = m_\pi^{(\rm vs)}$). In that case, only one analytic counterterm is needed for each coupling, and we removed the terms $c_i^{(\rm vs)}[m_\pi^{(\rm vs)}]^2$ from Eqs. (87)–(89). These fits, again using $n_{\rm HYP} = 1, 2, 3$, then gave $g_1 = 0.467 \pm 0.056$, $g_2 = 0.92 \pm 0.22$, and $g_3 = 0.72 \pm 0.14$, in full agreement with (90) and (91) and with slightly larger uncertainties.

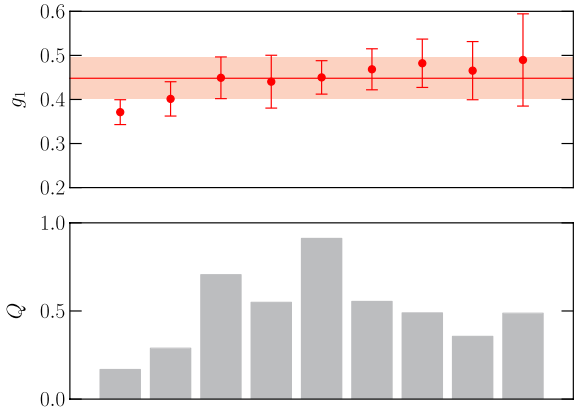

FIG. 7 (color online). Graphical representation of the fit results for g_1 from Table VI. The horizontal axis corresponds to the different fits, ordered (from left to right) in the same way as the rows in the table (from top to bottom). The line and shaded region in the upper plot indicate the selected result and its uncertainty, which is taken from the third fit (the fit that includes data with $n_{\rm HYP} = 1, 2, 3$).

Plots of the functions $(g_1)_{\rm eff}$, $(g_2)_{\rm eff}$, and $(g_3)_{\rm eff}$, with the parameters from the fits including the complete data with $n_{\rm HYP} = 1, 2, 3$ [i.e., the fit that gives the results (90) and (91)] are shown in Figs. 10–12. For the figures, the functions were evaluated in infinite volume, for the lattice spacings $a = 0.112$ fm, $a = 0.085$ fm, and $a = 0$. The right-hand sides of the figures show the values and uncertainties of the fitted functions for the unitary case $m_\pi^{(\rm vv)} = m_\pi^{(\rm vs)}$, while the left-hand sides show the dependence on both $m_\pi^{(\rm vv)}$ and $m_\pi^{(\rm vs)}$. At the two nonzero values of a, the functions were evaluated for $n_{\rm HYP} = 3$ and the corresponding data points are also shown (in the continuum limit, the functions for $n_{\rm HYP} = 1, 2, 3$ are all equal). To allow the inclusion in these plots, the data points were shifted to infinite volume using

$$\begin{aligned}(g_i)_{\rm eff,data}(m, L = \infty) = (g_i)_{\rm eff,data}(m, L = 2.7\ \text{fm}) \\ + [(g_i)_{\rm eff,fit}(m, L = \infty) \\ - (g_i)_{\rm eff,fit}(m, L = 2.7\ \text{fm})],\end{aligned} \tag{93}$$

where we use the notation $m = (m_\pi^{(\rm vv)}, m_\pi^{(\rm vs)})$. The numerical values of the volume shifts are given in Table VIII. The largest volume shift (2.8%) occurred for $(g_2)_{\rm eff}$ at $m_\pi^{(\rm vv)} = 227$ MeV.

The functions $(g_2)_{\rm eff}$ and $(g_3)_{\rm eff}$ develop small imaginary parts for pion masses below the $S \to T\pi$ threshold at $m_\pi = \Delta$ [20] (the lattice data are all above the threshold). The extracted parameters $g_{1,2,3}$ are real. Figs. 11 and 12

TABLE VII. Results for the baryonic axial couplings g_2 and g_3, obtained by simultaneously fitting the data for $(g_2)_{\text{eff}}$ and $(g_3)_{\text{eff}}$ using the functions (88) and (89). The first four rows show the results from fits which include data with multiple values of the heavy-quark smearing parameter n_{HYP}. The remaining rows show the results from fits with only one value of n_{HYP}. The number of degrees of freedom (d.o.f.) is given in the form (number of data points)—(number of fit parameters). The last column of the table gives the quality of the fit $Q = \Gamma(\text{d.o.f.}/2, \chi^2/2)$.

n_{HYP}	g_2	g_3	d.o.f.	χ^2/d.o.f.	Q
1, 2, 3, 5, 10	0.72(12)	0.635(90)	58 − 16	0.94	0.57
1, 2, 3, 5	0.73(13)	0.61(11)	46 − 14	1.1	0.31
1, 2, 3	0.84(20)	0.71(12)	34 − 12	0.61	0.92
1, 2	0.81(22)	0.57(17)	22 − 10	0.50	0.91
10	0.90(15)	0.75(11)	12 − 8	0.64	0.64
5	0.98(19)	0.76(13)	12 − 8	0.74	0.57
3	0.98(23)	0.74(15)	12 − 8	0.54	0.71
2	0.91(23)	0.66(18)	12 − 8	0.51	0.67
1	0.79(29)	0.61(27)	12 − 8	0.42	0.74

show the real parts of $(g_2)_{\text{eff}}$ and $(g_3)_{\text{eff}}$ only, which have kinks at the thresholds.

The fit results for the parameters $c_i^{(\text{vv})}$, $c_i^{(\text{vs})}$, which describe the analytic contributions, were natural-sized, i.e., of order $1/\Lambda_\chi^2$ with $\Lambda_\chi \approx 4\pi f_\pi$, for the renormalization scale $\mu = 4\pi f_\pi$. The fit results for the parameters $d_{i,n_{\text{HYP}}}$, which describe the lattice-spacing dependence, were also of natural size and consistent with zero within the statistical uncertainties. The absence of significant a dependence can also be seen in Figs. 10–12.

The individual contributions from different classes of Feynman diagrams in HHχPT [20] to the fitted functions $(g_1)_{\text{eff}}$, $\Re[(g_2)_{\text{eff}}]$, and $\Re[(g_3)_{\text{eff}}]$ (evaluated for $a = 0$, $L = \infty$, and $m_\pi^{(\text{vv})} = m_\pi^{(\text{vs})}$) are shown in Figs. 13 and 14. Note that while the sum of all contributions (including the analytic terms) is independent of the renormalization scale μ, the individual contributions are not, and the figures are based on the natural scale $\mu = 4\pi f_\pi$. For the range of pion masses considered here, the next-to-leading-order (NLO) contributions are significantly smaller than the leading-order contribution (which is equal to g_i). This, and the natural size of the fitted coefficients $c_i^{(\text{vv})}$, $c_i^{(\text{vs})}$, indicates that the chiral expansion of the axial-current matrix elements is well-behaved here.

To estimate the size of systematic uncertainties caused by the missing next-to-next-to-leading-order (NNLO) terms in the fits to the quark-mass and lattice-spacing dependence, we performed fits to the data using modified functions $(g_i)_{\text{eff}}^{(\text{NLO+HO})}$ that include higher-order analytic terms,

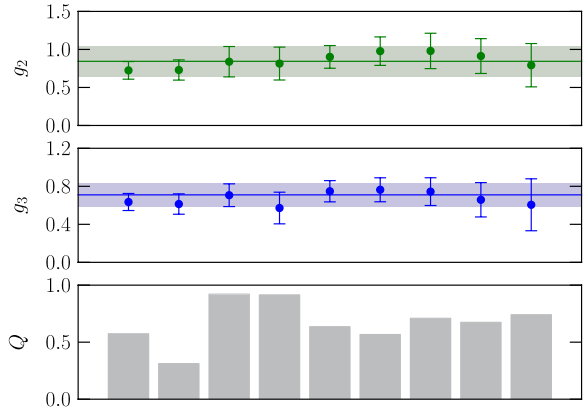

FIG. 8 (color online). Graphical representation of the fit results for g_2 and g_3 from Table VII. The horizontal axis corresponds to the different fits, ordered (from left to right) in the same way as the rows in the table (from top to bottom). The lines and shaded regions in the upper two plots indicate the selected results and their uncertainties, which are taken from the third fit (the fit that includes data with $n_{\text{HYP}} = 1, 2, 3$).

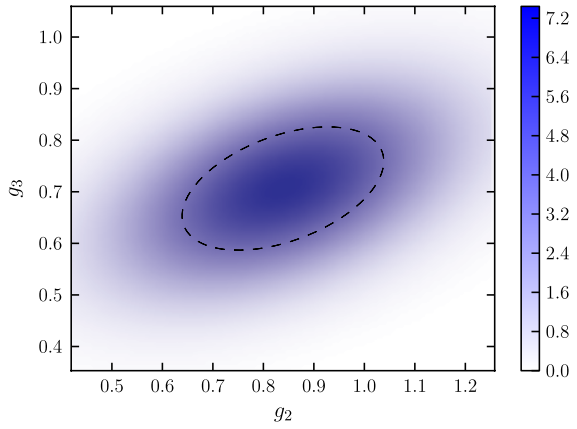

FIG. 9 (color online). Likelihood function for g_2 and g_3, equal to $L(g_2, g_3) = (2\pi)^{-1} \det(\text{Cov})^{-1/2} \exp\{-\frac{1}{2}(g_i - g_i^{(0)}) \times [\text{Cov}^{-1}]_{ij}(g_j - g_j^{(0)})\}$ where $g_i^{(0)}$ are the central values of our fit results (91) and Cov is the covariance matrix (92). The dashed curve indicates the standard error ellipse.

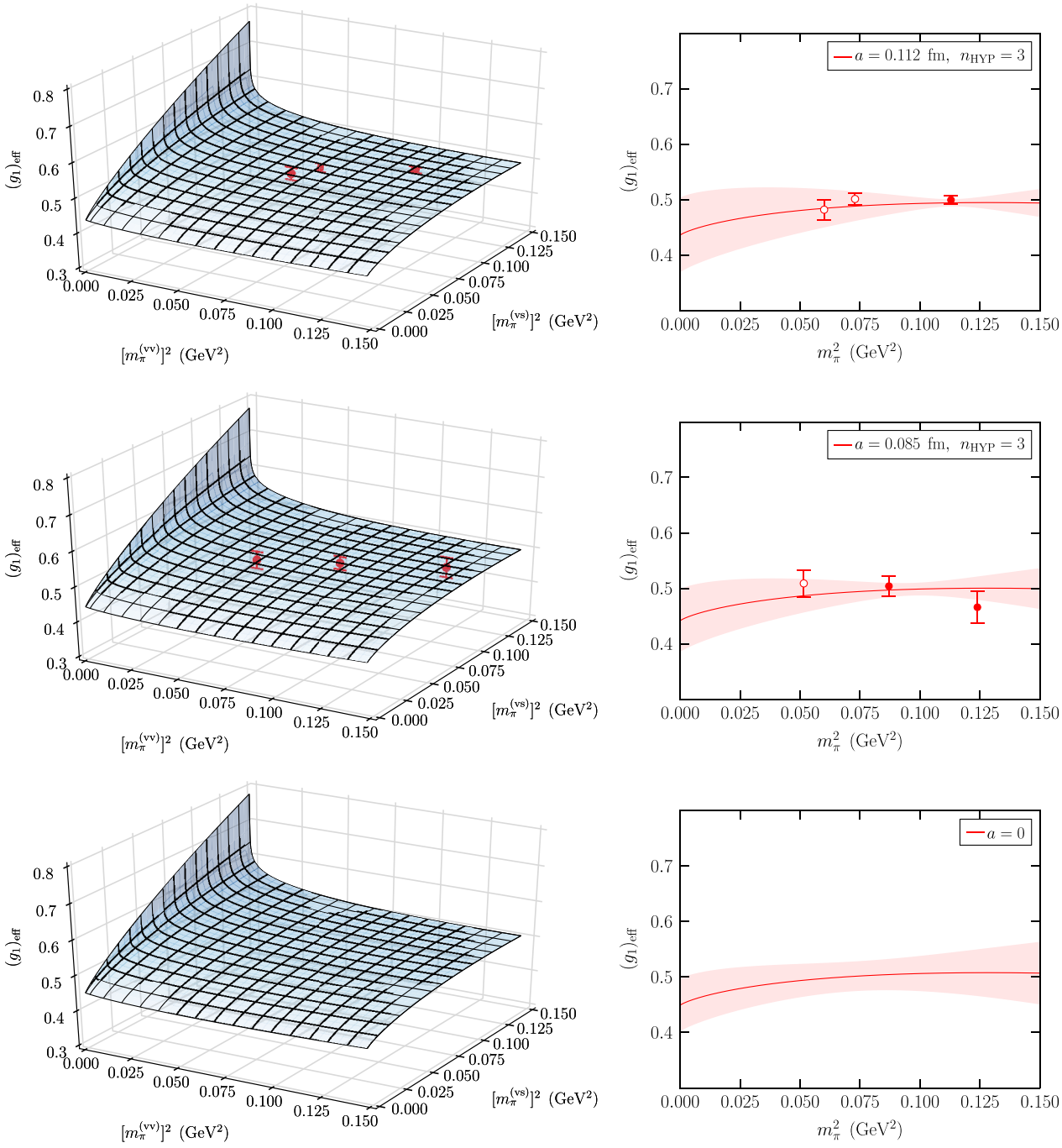

FIG. 10 (color online). The fitted function $(g_1)_{\rm eff}$, evaluated in infinite volume, for $n_{\rm HYP} = 3$, at different lattice spacings (from top to bottom: $a = 0.112$ fm, $a = 0.085$ fm, $a = 0$), along with the data points (shifted to infinite volume). The left-hand side shows the dependence on both $m_\pi^{(\rm vv)}$ and $m_\pi^{(\rm vs)}$. The right-hand side shows the function (and its statistical uncertainty) evaluated at $m_\pi^{(\rm vv)} = m_\pi^{(\rm vs)}$. In the plots on the right-hand side, the partially quenched data points, which have $m_\pi^{(\rm vv)} < m_\pi^{(\rm vs)}$, are indicated with open symbols. They are shown at $m_\pi = m_\pi^{(\rm vv)}$, even though the fitted function $(g_1)_{\rm eff}$ actually has slightly different values for these points.

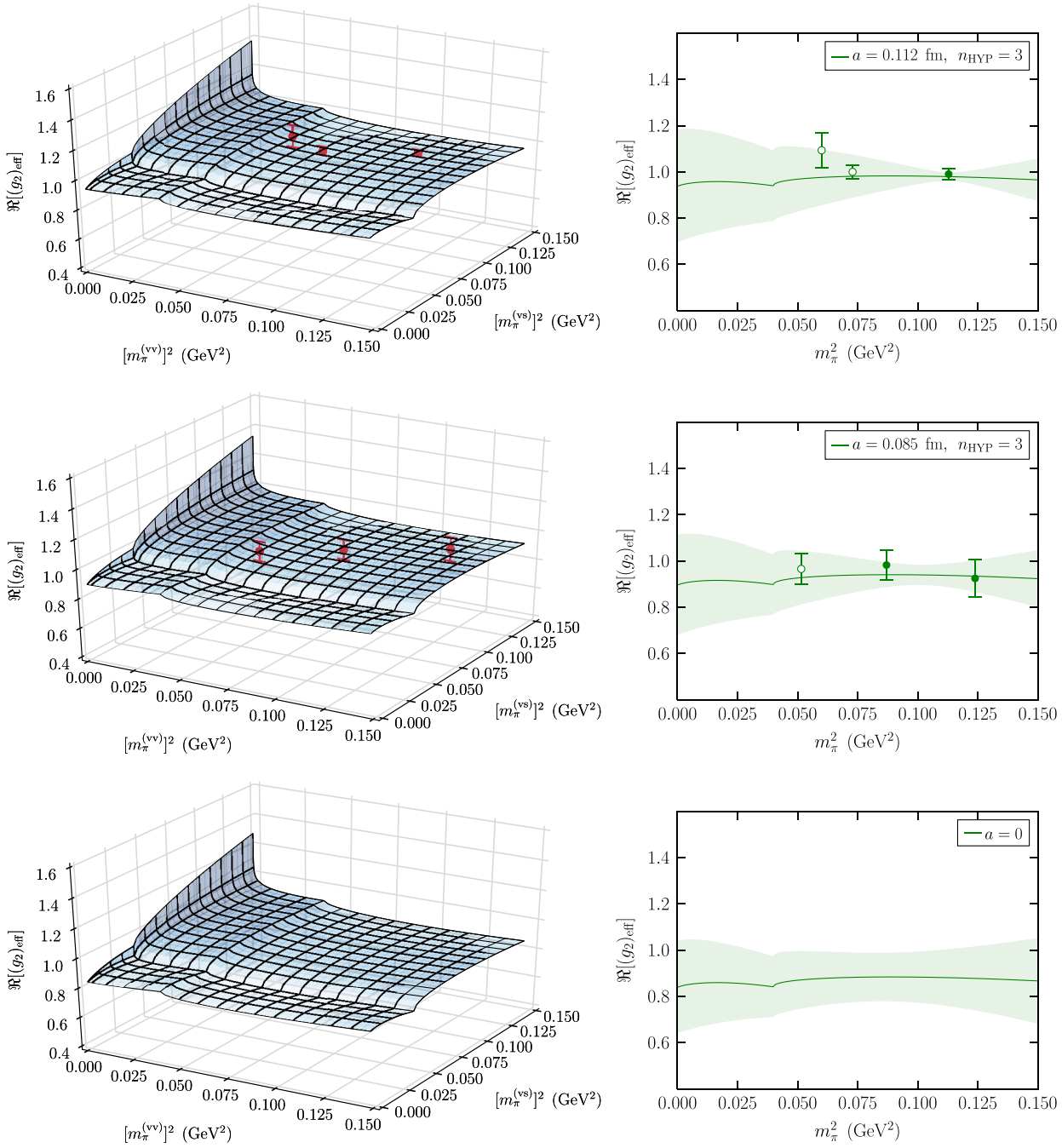

FIG. 11 (color online). Like Fig. 10, but for the real part of $(g_2)_{\rm eff}$.

$$
\begin{aligned}
&(g_i)_{\rm eff}^{(\rm NLO+HO)}(a, m, n_{\rm HYP}) \\
&= (g_i)_{\rm eff}^{(\rm NLO)}(a, m, n_{\rm HYP}) + g_i[c_i^{(\rm vv,vv)}[m_\pi^{(\rm vv)}]^4 \\
&\quad + c_i^{(\rm vs,vs)}[m_\pi^{(\rm vs)}]^4 + c_i^{(\rm vv,vs)}[m_\pi^{(\rm vv)}]^2[m_\pi^{(\rm vs)}]^2 \\
&\quad + d_{i,n_{\rm HYP}}^{(\rm vv)} a^2[m_\pi^{(\rm vv)}]^2 + d_{i,n_{\rm HYP}}^{(\rm vs)} a^2[m_\pi^{(\rm vs)}]^2 + h_{i,n_{\rm HYP}} a^4]. \quad (94)
\end{aligned}
$$

Here, the functions $(g_i)_{\rm eff}^{(\rm NLO)}$ are as defined in Eqs. (87)–(89). Because we do not have enough data to fit all the parameters in Eq. (94), we constrained the parameters corresponding to the higher-order terms using Gaussian priors centered around zero and with widths equal to some dimensionless factor w times the relevant natural scales

$$
\begin{aligned}
&c_i^{(\rm vv,vv)} = 0 \pm w/\Lambda_\chi^4, \qquad c_i^{(\rm vs,vs)} = 0 \pm w/\Lambda_\chi^4, \\
&c_i^{(\rm vv,vs)} = 0 \pm w/\Lambda_\chi^4, \qquad d_{i,n_{\rm HYP}}^{(\rm vv)} = 0 \pm w\Lambda_{\rm QCD}^2/\Lambda_\chi^2, \\
&d_{i,n_{\rm HYP}}^{(\rm vs)} = 0 \pm w\Lambda_{\rm QCD}^2/\Lambda_\chi^2, \qquad h_{i,n_{\rm HYP}} = 0 \pm w\Lambda_{\rm QCD}^4. \quad (95)
\end{aligned}
$$

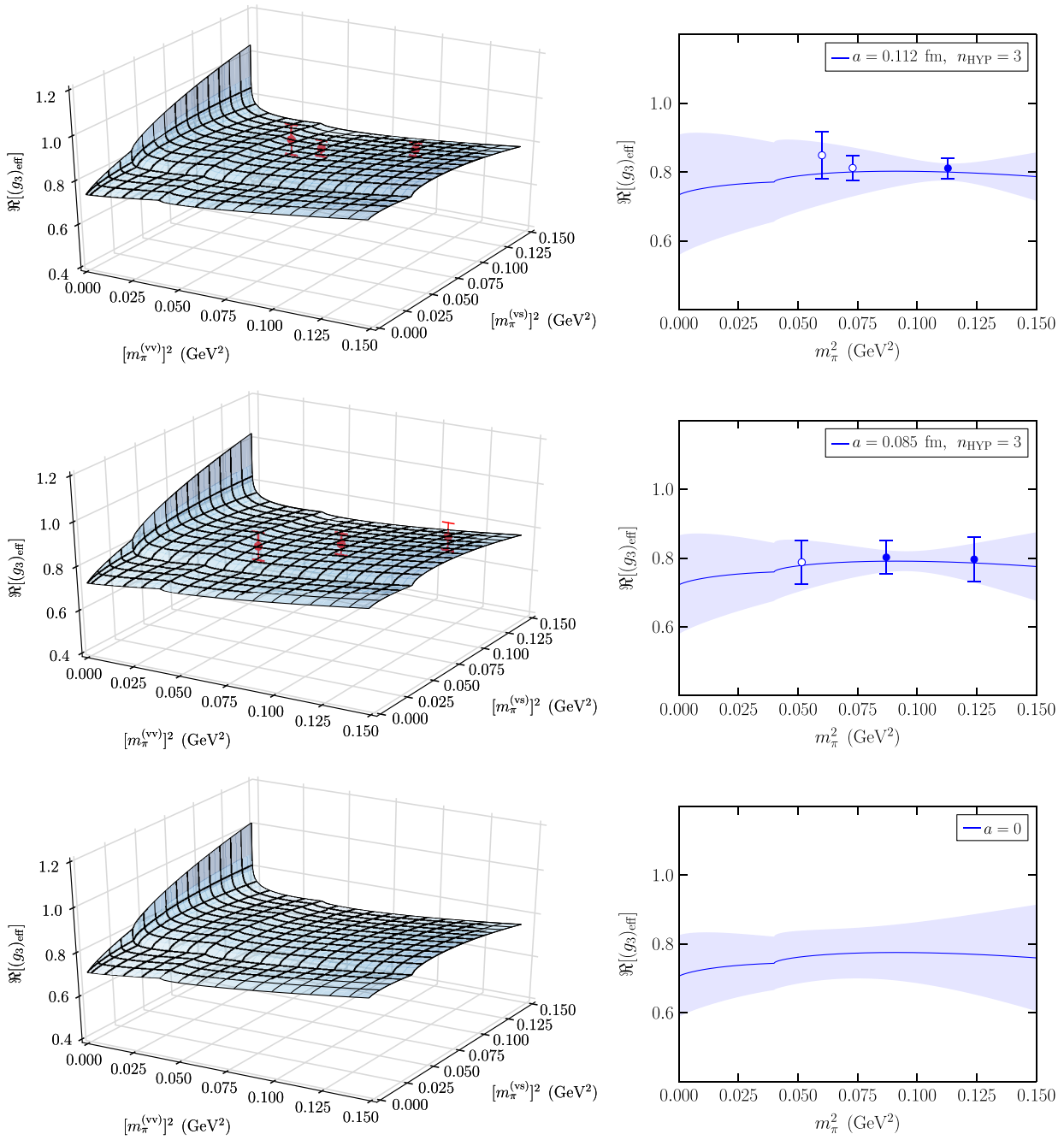

FIG. 12 (color online). Like Fig. 10, but for the real part of $(g_3)_{\rm eff}$.

TABLE VIII. Size of the finite-volume corrections for the pion masses where we have data.

$m_\pi^{(\rm vs)}$ (MeV)	$m_\pi^{(\rm vv)}$ (MeV)	$\frac{(g_1)_{\rm eff}^{(\infty)} - (g_1)_{\rm eff}^{(L)}}{(g_1)_{\rm eff}^{(\infty)}}$	$\frac{(g_2)_{\rm eff}^{(\infty)} - (g_2)_{\rm eff}^{(L)}}{(g_2)_{\rm eff}^{(\infty)}}$	$\frac{(g_3)_{\rm eff}^{(\infty)} - (g_3)_{\rm eff}^{(L)}}{(g_3)_{\rm eff}^{(\infty)}}$
294	245	0.0057	0.015	0.0074
304	270	0.0040	0.0070	0.0027
336	336	0.0016	0.00037	−0.00079
263	227	0.0072	0.028	0.013
295	295	0.0031	0.00027	−0.0012
352	352	0.0013	0.00033	−0.00071

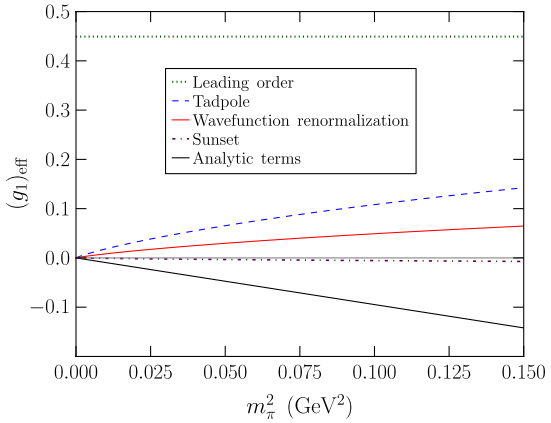

FIG. 13 (color online). Contributions from individual classes of Feynman diagrams in HHχPT (see Ref. [20]) to the fitted function $(g_1)_{\rm eff}$, evaluated in the infinite volume, continuum limit, for $m_\pi^{(\rm vv)} = m_\pi^{(\rm vs)}$. The renormalization scale is $\mu = 4\pi f$.

Here we used $\Lambda_\chi = 4\pi f_\pi$ with $f_\pi = 132$ MeV, and $\Lambda_{\rm QCD} = 300$ MeV. The fit results for the axial couplings g_i as a function of the width factor w are given in Table IX. While the case $w = 0$ corresponds to the original NLO fits, in the limit $w \to \infty$ the new parameters would become unconstrained (because we have insufficient data, we are unable to perform fits in this limit).

As can be seen in Table IX, the shifts in the central values of the axial couplings are smaller than the statistical errors up to the very large width $w = 100$. This is a consequence of the smallness of the quantities $m_\pi^4/(4\pi f_\pi)^4$, $a^2\Lambda_{\rm QCD}^2 m_\pi^2/(4\pi f_\pi)^2$, and $a^4\Lambda_{\rm QCD}^4$ for the pion masses and lattice spacings where we have data. The shifts in the central values fluctuate statistically and can be close to zero even for large w (at least for g_1). However, including the higher-order terms leads to a systematic increase in the uncertainties of the fit parameters g_i (as calculated from the Hessian of χ^2), as expected. Also shown in the table is the quantity

$$\delta\sigma(g_i) = \sqrt{\sigma^2(g_i)^{(\rm NLO+HO)} - \sigma^2(g_i)^{(\rm NLO)}}, \qquad (96)$$

where $\sigma(g_i)^{(\rm NLO)}$ is the original uncertainty of g_i from the NLO fit, and $\sigma(g_i)^{(\rm NLO+HO)}$ is the new uncertainty of g_i from the higher-order fit (95). To calculate (96) we used more digits for $\sigma(g_i)^{(\rm NLO)}$ and $\sigma(g_i)^{(\rm NLO+HO)}$ than shown in Table IX. Equation (96) gives the additional uncertainty in g_i, calculated using quadrature, that results from the higher-order terms. This additional uncertainty $\delta\sigma(g_i)$ scales roughly linearly with the width parameter w. For a reasonable choice of w, the quantity $\delta\sigma(g_i)$ can be considered to be the systematic uncertainty in g_i from the NLO fit due to the missing NNLO terms. Here we choose the conservative value of $w = 10$ for this purpose. The resulting estimates of relative systematic uncertainties can be found in Table X. There, we also show the estimates of the other relevant sources of uncertainties: effects of higher excited states in the fits to $R_i(t)$ as discussed in Sec. IV B, and the effects the sea-strange-quark mass being about 10% above the physical value, as discussed in Sec. III. Including the estimates of the total systematic uncertainties, our final results for the axial couplings, based on (90) and (91), are then

$$\begin{aligned} g_1 &= 0.449 \pm 0.047_{\rm stat} \pm 0.019_{\rm syst} = 0.449 \pm 0.051, \\ g_2 &= 0.84 \pm 0.20_{\rm stat} \pm 0.04_{\rm syst} = 0.84 \pm 0.20, \\ g_3 &= 0.71 \pm 0.12_{\rm stat} \pm 0.04_{\rm syst} = 0.71 \pm 0.13. \end{aligned} \qquad (97)$$

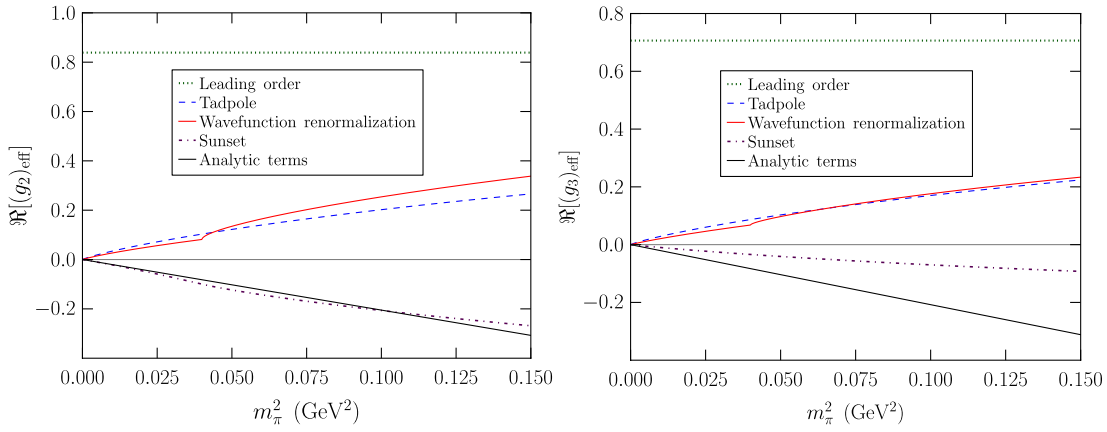

FIG. 14 (color online). Contributions from individual classes of Feynman diagrams in HHχPT (see Ref. [20]) to the real part of the fitted functions $(g_2)_{\rm eff}$ (left panel) and $(g_3)_{\rm eff}$ (right panel), evaluated in the infinite volume, continuum limit, for $m_\pi^{(\rm vv)} = m_\pi^{(\rm vs)}$. The renormalization scale is $\mu = 4\pi f$.

TABLE IX. Results of higher-order fits using Eq. (94) as a function of the width factor w defined in Eq. (95).

w	g_1	$\delta\sigma(g_1)$	g_2	$\delta\sigma(g_2)$	g_3	$\delta\sigma(g_3)$
0	0.449(47)	0	0.84(20)	0	0.71(12)	0
1	0.449(47)	0.0020	0.84(20)	0.0023	0.71(12)	0.0045
5	0.452(48)	0.0089	0.84(20)	0.014	0.70(12)	0.017
10	0.455(50)	0.016	0.84(20)	0.024	0.70(12)	0.026
50	0.464(72)	0.054	0.82(22)	0.099	0.68(15)	0.094
100	0.452(94)	0.082	0.78(26)	0.17	0.63(21)	0.17

TABLE X. Estimates of systematic uncertainties in the axial couplings g_i.

Source	g_1	g_2	g_3
NNLO terms in fits of m_π and a dependence	3.6%	2.8%	3.7%
Higher excited states in fits to $R_i(t)$	1.7%	2.8%	4.9%
Unphysical value of $m_s^{(\mathrm{sea})}$	1.5%	1.5%	1.5%
Total	4.2%	4.3%	6.3%

V. COMPARISON WITH PREVIOUS RESULTS FOR THE AXIAL COUPLINGS

We begin this section by discussing previous lattice calculations of the heavy-meson axial-current matrix elements and the corresponding extractions of g_1. A summary of results is shown in Table XI. All of the past works used an order-a improved Wilson action [42] for the light quarks, and variants of the Eichten-Hill action [22,23] for the static heavy quark. The first lattice estimate for g_1 was obtained in the pioneering work of Ref. [14], using a $12^3 \times 24$ lattice and quenched gauge fields, where the fermion determinants in the path-integral weight are set to 1, which means that the vacuum-polarization effects of the light quarks are neglected. In Ref. [14], the average of $(g_1)_{\mathrm{eff}}$ from two different valence pion masses (760 MeV, 900 MeV) was taken as the result for g_1. Quenched calculations of g_1 were also reported in Refs. [15,16]. The results for g_1 in these works were obtained by extrapolating data for $(g_1)_{\mathrm{eff}}$, at pion masses in the range of about 550 to 850 MeV, linearly in $[m_\pi^{(\mathrm{vv})}]^2$ to $m_\pi^{(\mathrm{vv})} = 0$.

Since calculations without sea quarks have uncontrolled systematic errors, more recent lattice calculations of g_1 have been performed with dynamical flavors, albeit only for $n_f = 2$. The first of these was done in Ref. [17], using two different lattices of sizes $12^3 \times 24$ and $16^3 \times 32$, and pion masses in the range 490—1100 MeV. Stochastic all-to-all propagators were used to reduce the statistical uncertainties. In Ref. [17], the data for the axial-current matrix elements $(g_1)_{\mathrm{eff}}$ was fitted using different approaches: linear in m_π^2, linear + quadratic in m_π^2, or linear + quadratic + logarithmic in m_π^2, using the average of g_1 from the linear and the linear + quadratic + logarithmic fits as the final result. A second unquenched calculation was published in Ref. [18], using three different lattice spacings and pion masses in the range from 400 to 1100 MeV. In Ref. [18], the coupling g_1 was obtained from a linear+logarithmic fit of $(g_1)_{\mathrm{eff}}$. Recently, the axial couplings of orbitally excited heavy-light mesons were also included [43]. Another $n_f = 2$ calculation of g_1 was reported in Ref. [19], with three different lattice spacings and pion masses down to 250 MeV. In Ref. [19], the result of an extrapolation of $(g_1)_{\mathrm{eff}}$ linear in m_π^2 was given as the value of g_1.

The coefficient of the chiral logarithm used in the fits of the axial-current matrix elements $(g_1)_{\mathrm{eff}}$ in Refs. [17,18]

TABLE XI. Comparison of lattice QCD results for the mesonic axial coupling g_1. Also shown are the numbers of dynamical light-quark flavors n_f, the fermion lattice action, and the range of valence pion masses used in the calculation.

Reference	n_f, action	$[m_\pi^{(\mathrm{vv})}]^2$ (GeV^2)	g_1
De Divitiis *et al.*, 1998 [14]	0, clover	0.58–0.81	$0.42 \pm 0.04 \pm 0.08$
Abada *et al.*, 2004 [15]	0, clover	0.30–0.71	$0.48 \pm 0.03 \pm 0.11$
Negishi *et al.*, 2007 [16]	0, clover	0.43–0.72	0.517 ± 0.016
Ohki *et al.*, 2008 [17]	2, clover	0.24–1.2	$0.516 \pm 0.005 \pm 0.033 \pm 0.028 \pm 0.028$
Bećirević *et al.*, 2009 [18]	2, clover	0.16–1.2	$0.44 \pm 0.03^{+0.07}_{-0.00}$
Bulava *et al.*, 2010 [19]	2, clover	0.063–0.49	0.51 ± 0.02
This work	2 + 1, domain wall	0.052–0.12	$0.449 \pm 0.047_{\mathrm{stat}} \pm 0.019_{\mathrm{syst}}$

was set equal to that of the strong-decay $P^* \to P\pi$ in $SU(2)$ HHχPT [44], because the corresponding loop contributions for the axial-current matrix elements were not known at that time. The NLO expression for the strong-decay amplitude in $SU(2)$ HHχPT is proportional to

$$\mathcal{M}(P^* \to P\pi) \propto g_1\left[1 - 4g_1^2\frac{m_\pi^2}{(4\pi f_\pi)^2}\log\frac{m_\pi^2}{\mu^2} + \tilde{c}m_\pi^2\right]. \tag{98}$$

We have recently derived the NLO expressions for the axial-current matrix elements in $SU(2)$, $SU(3)$, $SU(4|2)$, and $SU(6|3)$ HHχPT [20]. As discussed in Ref. [20], the chiral expansion of the axial-current matrix elements contains an additional tadpole loop contribution, which modifies the coefficient of the logarithm. In the $SU(2)$ case, one has

$$(g_1)_{\text{eff}} = g_1\left[1 - (2 + 4g_1^2)\frac{m_\pi^2}{(4\pi f_\pi)^2}\log\frac{m_\pi^2}{\mu^2} + cm_\pi^2\right]. \tag{99}$$

Because $g_1 \approx 0.5$, the coefficient of the logarithm in Eq. (99) is numerically about 3 times larger than the coefficient of the logarithm in Eq. (98). The logarithm makes $(g_1)_{\text{eff}}$ as a function of m_π^2 curve downward when m_π^2 is decreased (see Fig. 10). The results for g_1 from the previous unquenched lattice calculations, which incorrectly used Eq. (98) or did not include any logarithm in the fits, would be significantly lower if the correct HHχPT formula (99) had been used instead. We have attempted fits to the data of [17–19] using Eq. (99), obtaining values of g_1 that are about 10 to 20% lower than what is published in these works. Note, however, that HHχPT is not expected to converge in the upper range of the pion masses in [17,18]. For the data used in the present work, incorrect fits linear in m_π^2 or using Eq. (98) give values for g_1 that are higher than the correct result, Eq. (90), by 12% and 8%, respectively.

Next, we move to the discussion of various theoretical estimates of the axial couplings g_1, g_2, g_3 based on approximations, models, and experimental data. A comparison of these estimates to our QCD results is shown in Table XII. The nonrelativistic quark model (NRQM) predicts $g_1 = g_A^{ud}$, $g_2 = 2g_A^{ud}$ and $g_3 = \sqrt{2}g_A^{ud}$ [5], where $g_A^{ud} = 1$ is the axial coupling of the single-quark transition $u \to d$. Interestingly, if g_A^{ud} is set to 0.75, the value needed to reproduce the experimental value of the nucleon axial charge, one obtains $g_1 = 0.75$, $g_2 = 1.5$, $g_3 = 1.06$, still significantly larger than our QCD results. The predicted *ratios* of the axial couplings in the NRQM are, however, consistent with our lattice determination. The relativistic quark models of Refs. [45,46] give $g_1 = 1/3$ and $g_1 = 0.6 \pm 0.1$, respectively.

Another theoretical approach for estimating the axial couplings is the large-N_c limit of QCD, where N_c is the number of colors. In the limit $N_c \to \infty$, one finds that the baryonic couplings satisfy the relation [47,57]

$$\left.\frac{g_2}{g_3}\right|_{N_c=\infty} = \sqrt{\frac{3}{2}} \approx 1.22. \tag{100}$$

For comparison, our lattice QCD result for this ratio is

$$\frac{g_2}{g_3} = 1.19(26), \tag{101}$$

TABLE XII. Comparison of our lattice QCD results for the axial couplings g_1, g_2, and g_3 with other determinations as reported in the literature [all results are shown in our normalization, see Eq. (11)]. Here, NRQM stands for nonrelativistic quark model. Where decay widths or branching fractions are listed under "Method", these are experimental inputs. As discussed in the main text, the axial couplings extracted from experimental data are defined away from the static limit in some cases. When a reference contained multiple results for the same coupling and did not specify which one is the most reliable, we quote here the range from the lowest result minus its uncertainty up to the highest result plus its uncertainty.

Reference	Method	g_1	g_2	g_3
Yan *et al.*, 1992 [5]	Nonrelativistic quark model	1	2	$\sqrt{2}$
Colangelo *et al.*, 1994 [45]	Relativistic quark model	1/3	…	…
Bećirević, 1999 [46]	Quark model with Dirac eq.	0.6 ± 0.1	…	…
Guralnik *et al.*, 1992 [47]	Skyrme model	…	1.6	1.3
Colangelo *et al.*, 1994 [48]	Sum rules	0.15–0.55	…	…
Belyaev *et al.*, 1994 [49]	Sum rules	0.32 ± 0.02	…	…
Dosch and Narison, 1995 [50]	Sum rules	0.15 ± 0.03	…	…
Colangelo and Fazio, 1997 [51]	Sum rules	0.09–0.44	…	…
Pirjol and Yan, 1997 [52]	Sum rules	…	$<\sqrt{6 - g_3^2}$	$<\sqrt{2}$
Zhu and Dai, 1998 [53]	Sum rules	…	$1.56 \pm 0.30 \pm 0.30$	$0.94 \pm 0.06 \pm 0.20$
Cho and Georgi, 1992 [54]	$\mathcal{B}[D^* \to D\pi]$, $\mathcal{B}[D^* \to D\gamma]$	0.34 ± 0.48	…	…
Arnesen *et al.*, 2005 [55]	$\mathcal{B}[D^*_{(s)} \to D_{(s)}\pi]$, $\mathcal{B}[D^*_{(s)} \to D_{(s)}\gamma]$, $\Gamma[D^*]$	0.51	…	…
Li *et al.*, 2010 [56]	$d\Gamma[B \to \pi\ell\nu]$	<0.87	…	…
Cheng, 1997 [30]	$\Gamma[\Sigma_c^* \to \Lambda_c\pi]$, NRQM	0.70 ± 0.12	1.40 ± 0.24	0.99 ± 0.17
This work	Lattice QCD	0.449 ± 0.051	0.84 ± 0.20	0.71 ± 0.13

and the nonrelativistic quark model predicts $g_2/g_3 = \sqrt{2} \approx 1.41$.

The axial couplings have also been estimated using sum rules [48–53], with results as shown in Table XII. For the heavy-meson coupling g_1, most sum rule determinations are smaller than our lattice QCD result, and much smaller than the NRQM value. In contrast, the values of g_2 and g_3 obtained using sum rules in Ref. [53] are larger than our lattice results.

Experimental data for various heavy-hadron decay processes has also been used to determine the axial couplings. In Ref. [54], electromagnetic interactions were included in HHχPT, and the coupling g_1 was extracted from the measured branching fractions $\mathcal{B}[D^* \to D\pi]$ and $\mathcal{B}[D^* \to D\gamma]$ at tree level, finding $g_1 = 0.43 \pm 0.61$ for $m_c = 1.5$ GeV and $g_1 = 0.34 \pm 0.48$ for $m_c = 1.7$ GeV. Note that these values for g_1 are not defined in the static limit; they are effective values corresponding to the $D^*D\pi$ coupling. A similar calculation, which additionally included the leading nonanalytic effects in the radiative decays, is reported in Ref. [58]. The complete $1/m_Q$ and loop corrections in both the strong and radiative decays were included in the analysis of Ref. [59]. There, the fit to experimental data for the branching fractions $\mathcal{B}[D^*_{(s)} \to D_{(s)}\pi]$ and $\mathcal{B}[D^*_{(s)} \to D_{(s)}\gamma]$ gave two possible solutions for g_1. The fit of Ref. [59] was updated later by including experimental results for $\Gamma[D^*]$ [60], leading to $g_1 \simeq 0.51$ [55], where (unlike in Ref. [59]) g_1 is defined in the static limit.

Recently, g_1 was also extracted from data for the $B \to \pi\ell\nu$ form factors, giving results for g_1 in the range from 0.02 ± 0.32 up to $0.73^{+0.14}_{-0.12}$ depending on the parametrizations of the form factor shape [56]. The measured widths of the baryonic decays $\Sigma_c^* \to \Lambda_c\pi$ were used in Refs. [30,52] to estimate g_3, with the result 0.99 ± 0.17. The NRQM relations then give $g_1 = g_3/\sqrt{2} = 0.70 \pm 0.12$ and $g_2 = g_3/2 = 1.40 \pm 0.24$ [30]. However, as discussed in Sec. VI, the value of "g_3" extracted directly from $\Gamma[\Sigma_c^* \to \Lambda_c\pi]$ should really be considered as an effective value of the decay coupling constant at $m_Q = m_c$, deviating from the static-limit axial coupling by corrections of order $\Lambda_{\rm QCD}/m_c \sim 30\%$.

VI. CALCULATION OF DECAY WIDTHS

In this section, we use our lattice QCD results for the axial couplings g_2 and g_3 to calculate various decay widths of heavy baryons. At leading order in the chiral expansion, the widths for the strong decays $S \to T\pi$ are

$$\Gamma[S \to T\pi] = c_{\rm f}^2 \frac{1}{6\pi f_\pi^2}\left(g_3 + \frac{\kappa_J}{m_Q}\right)^2 \frac{M_T}{M_S}|\mathbf{p}_\pi|^3, \quad (102)$$

where S and T now denote physical $s_l = 1$ and $s_l = 0$ heavy-baryon states such as Σ_b and Λ_b, $|\mathbf{p}_\pi|$ is the magnitude of the pion momentum in the S rest frame,

$$|\mathbf{p}_\pi| = \frac{\sqrt{[(M_S - M_T)^2 - m_\pi^2][(M_S + M_T)^2 - m_\pi^2]}}{2M_S}, \quad (103)$$

and $c_{\rm f}$ is a flavor factor [61],

$$c_{\rm f} = \begin{cases} 1 & \text{for } \Sigma_Q^{(*)} \to \Lambda_Q\pi^\pm, \\ 1 & \text{for } \Sigma_Q^{(*)} \to \Lambda_Q\pi^0, \\ 1/\sqrt{2} & \text{for } \Xi_Q^{\prime(*)} \to \Xi_Q\pi^\pm, \\ 1/2 & \text{for } \Xi_Q^{\prime(*)} \to \Xi_Q\pi^0. \end{cases} \quad (104)$$

The $m_Q = \infty$ expression for Γ can be found, for example, in [52]. In Eq. (102), we included the term κ_J/m_Q to account for the first-order corrections for a finite heavy-quark mass. The parameters κ_J are related to the additional couplings in the order-$1/m_Q$ HHχPT Lagrangian [62]. Terms suppressed by $(m_\pi/\Lambda_\chi)^2$ and $(\Lambda_{\rm QCD}/m_Q)^2$, which are omitted from (102), lead to small systematic uncertainties in Γ.

To determine $\kappa_{1/2}$ and $\kappa_{3/2}$, we performed fits of experimental data [63] for the widths of the Σ_c^{++}, Σ_c^0 ($J = 1/2$) and the Σ_c^{*++}, Σ_c^{*0} ($J = 3/2$) using (102), where we constrained g_3 to our lattice QCD result (97) and set $m_Q = \frac{1}{2}M_{J/\psi}$. These fits are shown in Fig. 15 and gave the results

$$\begin{aligned} \kappa_{1/2} &= 0.55(21)\ \text{GeV}, \\ \text{Cov}(\kappa_{1/2}, g_3) &= -0.025\ \text{GeV}, \\ \kappa_{3/2} &= 0.47(21)\ \text{GeV}, \\ \text{Cov}(\kappa_{3/2}, g_3) &= -0.025\ \text{GeV}. \end{aligned} \quad (105)$$

The fit parameters κ_J are correlated with g_3, and therefore we also show the covariances in Eq. (105). The value of the sum $g_3 + \frac{\kappa_J}{m_Q}$ in Eq. (102) is plotted as a function of $1/m_Q$ in Fig. 16. For $m_Q = \frac{1}{2}M_{J/\psi}$, the values of $g_3 + \frac{\kappa_J}{m_Q}$

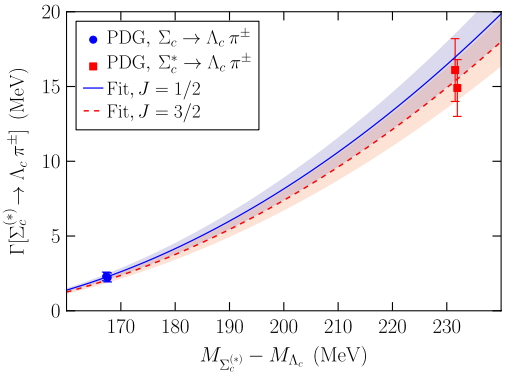

FIG. 15 (color online). Experimental data for $\Gamma[\Sigma_c^{(*)} \to \Lambda_c\pi^\pm]$ from Ref. [63], along with fits using Eq. (102), for $J = 1/2$ (solid curve) and $J = 3/2$ (dashed curve).

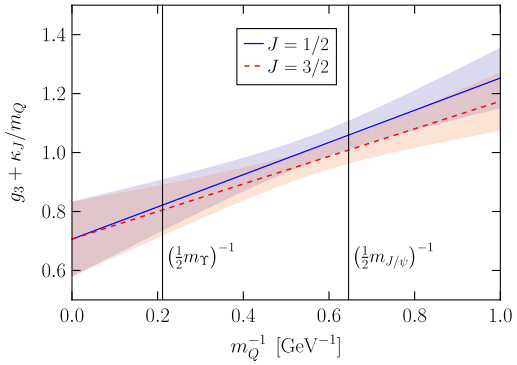

FIG. 16 (color online). Value and uncertainty of the quantity $(g_3 + \kappa_J/m_Q)$, which enters in the strong-decay width (102), as a function of the inverse heavy-quark mass m_Q^{-1}, for $J = 1/2$ (solid curve) and $J = 3/2$ (dashed curve). At $m_Q^{-1} = 0$ the function is equal to g_3, which is given by our lattice QCD result (97). The vertical lines indicate our choices for the inverse bottom and charm quark masses.

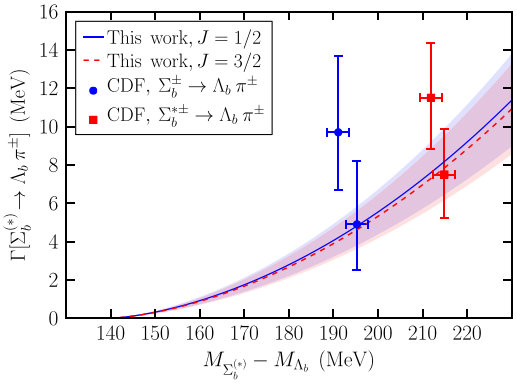

FIG. 17 (color online). Widths of the decays $\Sigma_b^{(*)\pm} \to \Lambda_b \pi^{\pm}$ as functions of the $\Sigma_b^{(*)} - \Lambda_b$ mass difference. The curves (solid: Σ_b, dashed: Σ_b^*) and shaded regions show our predictions and their uncertainties. The experimental data points are from CDF [13].

are determined dominantly by the experimental input used to fit κ_J,

$$g_3 + \frac{\kappa_{1/2}}{\frac{1}{2}m_{J/\psi}} = 1.059(49), \quad g_3 + \frac{\kappa_{3/2}}{\frac{1}{2}m_{J/\psi}} = 1.008(46). \tag{106}$$

Using the masses of the Ξ_c^* and Ξ_c baryons from Ref. [63], we obtain predictions for $\Gamma[\Xi_c^{*+} \to \Xi_c^+ \pi^0, \Xi_c^0 \pi^+]$ and $\Gamma[\Xi_c^{*0} \to \Xi_c^0 \pi^0, \Xi_c^+ \pi^-]$ as shown in Table XIII. There, we also show other predictions from the literature, as well as upper limits from experiments [71,72]. Our results for $\Gamma[\Xi_c^{*+}]$ and $\Gamma[\Xi_c^{*0}]$ are compatible with these limits.

We can also make predictions for the radiative decay $\Xi_c^{*0} \to \Xi_c^0 \gamma$, which is forbidden at tree level but can be mediated by loops because of flavor-$SU(3)$ breaking. Using HHχPT, it has been shown that the branching fraction of this decay is related to the axial coupling g_2 as follows [73]:

$$\mathcal{B}[\Xi_c^{*0} \to \Xi_c^0 \gamma] = (1.0 \pm 0.3) \times 10^{-3} g_2^2. \tag{107}$$

Combining this with our lattice QCD result for g_2, Eq. (97), and our calculated strong-decay width $\Gamma[\Xi_c^{*0} \to \Xi_c^0 \pi^0, \Xi_c^+ \pi^-] = 2.78(29)$ MeV, we obtain

$$\begin{aligned} \mathcal{B}[\Xi_c^{*0} \to \Xi_c^0 \gamma] &= (7 \pm 4) \times 10^{-4}, \\ \Gamma[\Xi_c^{*0} \to \Xi_c^0 \gamma] &= (2.0 \pm 1.1) \text{ keV}. \end{aligned} \tag{108}$$

Next, we discuss the strong decays of bottom baryons. To calculate these widths, we evaluated (102) for $m_Q = \frac{1}{2}M_\Upsilon$. In this case the values of $g_3 + \frac{\kappa_J}{m_Q}$ are determined dominantly by the lattice result (97) for g_3,

$$g_3 + \frac{\kappa_{1/2}}{\frac{1}{2}m_\Upsilon} = 0.822(87), \qquad g_3 + \frac{\kappa_{3/2}}{\frac{1}{2}m_\Upsilon} = 0.805(87). \tag{109}$$

Our calculated widths $\Gamma[\Sigma_b^{(*)} \to \Lambda_b \pi^{\pm}]$ as functions of the $\Sigma_b^{(*)} - \Lambda_b$ mass difference are shown as the curves in Fig. 17. Using the experimental values of the baryon masses [13,63], we obtain the results for $\Gamma[\Sigma_b^{(*)} \to \Lambda_b \pi^{\pm}]$ shown in Table XIII, in agreement with the widths measured by the CDF collaboration [13].

In our previous work [21] we predicted that the widths of the Ξ_b' and Ξ_b^* are less than 1.1 and 2.8 MeV, respectively. Very recently, the CMS collaboration has observed the

TABLE XIII. Results in MeV for the total strong-decay widths of charm and bottom baryons.

Hadron	Ref. [52]	Ref. [64]	Ref. [61]	Ref. [65,66]	Ref. [67]	Ref. [68]	Ref. [69]	This work	Experiment
Σ_b^+	...	...	...	6.0	...	4.35	3.5	4.2(1.0)	$9.7^{+3.8+1.2}_{-2.8-1.1}$ [13]
Σ_b^-	...	...	...	7.7	...	5.77	4.7	4.8(1.1)	$4.9^{+3.1}_{-2.1} \pm 1.1$ [13]
Σ_b^{*+}	...	...	...	11.0	...	8.50	7.5	7.3(1.6)	$11.5^{+2.7+1.0}_{-2.2-1.5}$ [13]
Σ_b^{*-}	...	...	...	13.2	...	10.44	9.2	7.8(1.8)	$7.5^{+2.2+0.9}_{-1.8-1.4}$ [13]
Ξ_b^{*0}	...	...	...	...	...	...	0.85	0.51(16)	2.1 ± 1.7 [70]
Ξ_c^{*+}	1.2–4.1	1.81	3.04(37)	3.18(10)	2.7(2)	...	1.13	2.44(26)	<3.1(CL = 90%) [71]
Ξ_c^{*0}	1.2–4.0	1.88	3.12(33)	3.03(10)	2.8(2)	...	1.08	2.78(29)	<5.5(CL = 90%) [72]

Ξ_b^{*0}, finding a width of 2.1 ± 1.7 MeV [70].[1] The mass difference to the Ξ_b^- was measured to be

$$M_{\Xi_b^{*0}} - M_{\Xi_b^-} = 154.41 \pm 0.79 \text{ MeV}. \quad (110)$$

The Ξ_b^{*0} can decay into $\Xi_b^- \pi^+$ (seen by CMS) and into $\Xi_b^0 \pi^0$. Taking $M_{\Xi_b^-} - M_{\Xi_b^0} = 3.1 \pm 5.6 \pm 1.3$ MeV from the CDF measurement reported in Ref. [74], we have

$$M_{\Xi_b^{*0}} - M_{\Xi_b^0} = 157.5 \pm 5.8 \text{ MeV}. \quad (111)$$

Using the results (110) and (111), we can update our calculation of the Ξ_b^{*0} width and find

$$\Gamma[\Xi_b^{*0} \to \Xi_b^- \pi^+, \Xi_b^0 \pi^0] = 0.51 \pm 0.16 \text{ MeV}. \quad (112)$$

Given the observed mass difference (110), and assuming that $M_{\Xi_b^*} - M_{\Xi_b'} \approx M_{\Sigma_b^*} - M_{\Sigma_b} = 21 \pm 2$ MeV [29], it is likely that the decay $\Xi_b'^0 \to \Xi_b^- \pi^+$ is kinematically forbidden.

VII. CONCLUSIONS

The chiral dynamics of mesons and baryons containing a heavy quark is controlled at leading order by three axial couplings g_1, g_2, and g_3. Knowledge of the values of these couplings is an essential ingredient for precision QCD calculations in flavor physics. In this paper, we have discussed in detail the first complete lattice QCD determination of g_1, g_2, and g_3. We have extracted the axial couplings by fitting numerical data for matrix elements of the axial current using the quark-mass and volume dependence calculated in $SU(4|2)$ heavy-hadron chiral perturbation theory. Our final results are

$$\begin{aligned} g_1 &= 0.449 \pm 0.047_{\text{stat}} \pm 0.019_{\text{syst}}, \\ g_2 &= 0.84 \pm 0.20_{\text{stat}} \pm 0.04_{\text{syst}}, \\ g_3 &= 0.71 \pm 0.12_{\text{stat}} \pm 0.04_{\text{syst}}. \end{aligned} \quad (113)$$

The systematic uncertainties in (113) are very small, because our analysis is based on data at low pion masses, with a large volume, and at two different lattice spacings. We have also carefully removed the excited-state contamination in the matrix elements by extrapolating the ratios of correlation functions to infinite source-sink separation.

Previous lattice calculations of heavy-hadron axial couplings had only considered the mesonic coupling g_1. The early calculations of g_1 did not include dynamical quarks and hence are contaminated by uncontrolled systematic errors. The $n_f = 2$ calculations typically used large quark masses and the fits to the quark-mass dependence were performed either linearly in m_π^2 or with an incorrect coefficient of the chiral logarithm. Had the correct coefficient been used, significantly lower values of g_1 would have been obtained in these previous studies.

For the range of pion masses considered in our work ($230 \text{ MeV} \lesssim m_\pi \lesssim 350$ MeV), the chiral expansion of the axial-current matrix elements between heavy-light hadron states is found to be well-behaved. The next-to-leading-order contributions are small compared to the leading-order contributions, and NNLO contributions are negligible. The rapid convergence of the chiral expansion is also a consequence of the smallness of the static-light axial couplings (113). It is interesting to compare the chiral dynamics of hadrons containing a heavy quark with that of light baryons. Being particularly light, the interactions of virtual pions (and other pseudo-Goldstone bosons) produce significant contributions to many properties of baryons, and generically these effects scale quadratically with the strength with which a given baryon sources pions. This, in turn, is determined by the relevant axial coupling, $g_{1,2,3}$ in the case of heavy hadrons, and $g_A \approx 1.26$, $|g_{N\Delta}| \sim 1.6$ and $g_{\Delta\Delta} \sim -1.9$ in the case of light baryons [75,76]. From the numerical values of these couplings, it is apparent that chiral dynamics is more perturbative for heavy-light hadrons than that for light baryons.

Our results for the heavy-light axial couplings, Eq. (113), are significantly smaller than the values one obtains in the nonrelativistic quark-model, $g_1 = g_A^{ud}$, $g_2 = 2g_A^{ud}$ and $g_3 = \sqrt{2} g_A^{ud}$, where $g_A^{ud} = 1$ is the axial coupling of the single-quark transition $u \to d$. Even if g_A^{ud} is set to 0.75, as needed to reproduce the experimental value of the nucleon axial charge, the corresponding quark-model values of $g_{1,2,3}$ are still significantly smaller than the results (113) from first-principles lattice QCD.

We have used our results for g_2 and g_3 to calculate strong and radiative decay widths of charm and bottom baryons. For the strong decays, we have taken into account the order-$1/m_Q$ corrections, which we have constrained by combining experimental data for charmed baryon decay rates with our lattice determination of g_3. We found that the $1/m_Q$ corrections are significant (their effect on the amplitudes for $\Sigma_Q^{(*)} \to \Lambda_Q \pi$ decays is about 40% at $m_Q = m_c$ and about 13% at $m_Q = m_b$). As a consequence, the coupling g_3 cannot be reliably extracted from experimental data for charmed baryon decays alone, and our lattice calculation in the static limit is crucial to calculate the widths of bottom baryons. Our results for the widths of the $\Sigma_b^{(*)}$ baryons are in agreement with recent measurements at Fermilab.

Our determination of the axial couplings can also improve the precision of future lattice QCD calculations of other heavy-hadron properties such as masses, decay constants, and form factors, because the axial couplings control the dependence of these properties on the light-quark masses. Therefore, the calculation of the axial couplings from first principles also has an impact on searches for beyond-the-standard-model physics at the LHC and the planned SuperB experiment. Importantly, our results include the baryonic couplings g_2 and g_3. Heavy baryons may offer additional opportunities for probing the structure of new physics as a consequence of the different spin quantum numbers.

[1] Without a spin identification, there is a small possibility that the state observed by CMS is the $\Xi_b'^0$ instead. We do not consider this further.

ACKNOWLEDGMENTS

We would like to thank Hai-Yang Cheng, Kostas Orginos, Martin Savage, Brian Tiburzi, André Walker-Loud, and Matt Wingate for helpful discussions. We are indebted to the RBC and UKQCD collaborations for access to the gauge field configurations used in this work and to Robert Edwards and Balint Joó for the development of the CHROMA library [82] with which some of the calculations were performed. The work of W. D. is supported in part by Jefferson Science Associates, LLC, under U. S. Department of Energy Contract No. DE-AC05-06OR-23177 and by the Jeffress Memorial Trust, J-968. W. D. and S. M. were supported by DOE Outstanding Junior Investigator Award DE-SC000-1784 and DOE Grant No. DE-FG02-04ER41302. C. J. D. L. is supported by NSC Taiwan Grant No. 99-2112-M-009-004-MY3. We acknowledge the hospitality of Academia Sinica Taipei, National Chiao-Tung University, National Centre for Theoretical Sciences Taiwan, The College of William and Mary, and Thomas Jefferson National Accelerator Facility. This research made use of computational resources provided by NERSC and the NSF Teragrid (NCSA, TACC and NICS).

APPENDIX A: PLOTS OF RAW DATA

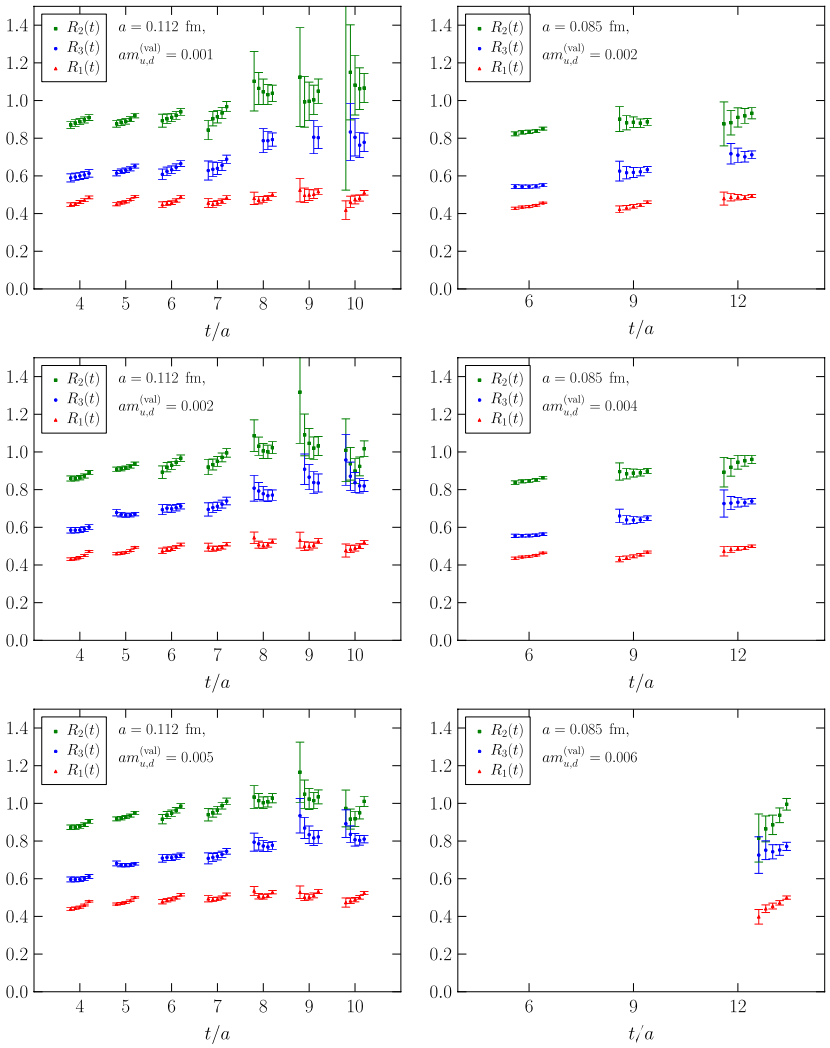

FIG. 18 (color online). Summary of all data points for $R_1(t)$, $R_2(t)$ and $R_3(t)$. At each value of t/a, results from up to five different values of n_{HYP} are shown (from left to right: $n_{\mathrm{HYP}} = 1, 2, 3, 5, 10$; points offset horizontally for legibility; in some cases there are no results for R_3 for the lowest values of n_{HYP}, because the statistical fluctuations were too large to calculate the square root of the double ratio). In physical units, the range of the horizontal axis in all plots is from $t = 0.336$ fm to $t = 1.23$ fm.

APPENDIX B: COMPARISON OF STANDARD RATIO METHOD AND SUMMATION METHOD

To extract the effective axial couplings from the ratios $R_i(t, t')$ defined in Eqs. (63)–(65), we defined $R_i(t)$ to be the average of $R_i(t, t')$ over a symmetric range of t' values around $t/2$ in a region where there was no discernible t' dependence, which essentially amounts to using

$$R_i(t, t/2). \tag{B1}$$

An alternative approach for extracting g_{eff} is the summation method [19,77–80]. In the following, we only consider the case of the simple ratios (63) and (64) for degenerate spectra. One defines the summed ratio $S_i(t)$ by summing $R_i(t, t')$ over all values of t',

$$S_i(t) = a \sum_{t'=0}^{t} R_i(t, t'). \tag{B2}$$

For large t, one expects [77,78]

$$S_i(t) \approx c_i + (g_i)_{\text{eff}} t, \tag{B3}$$

with some constant c_i. Thus, the coupling $(g_i)_{\text{eff}}$ can be extracted by taking the derivative [19,80],

$$R_i^{\text{sum}}(t) = \frac{d}{dt} S_i(t), \tag{B4}$$

which is approximated by a finite difference on the lattice. Assuming that there is a nonvanishing off-diagonal matrix element of the axial current between the ground-state hadron and an excited state with an energy gap δ (for our data, contamination from off-diagonal matrix elements actually appears to be very small, as discussed in Secs. IV A and IV B), one expects that the systematic uncertainties of (B1) and (B4) due to this excited state are of order [80]

$$\begin{aligned} R_i(t) - (g_i)_{\text{eff}} &= O(e^{-\frac{1}{2}\delta_i t}), \\ R_i^{\text{sum}}(t) - (g_i)_{\text{eff}} &= O(te^{-\delta_i t}) \end{aligned} \tag{B5}$$

[see Eq. (71) for the spectral decomposition of $R_i(t)$]. Thus, the excited-state contamination in $R_i^{\text{summed}}(t)$ decays effectively with twice the energy gap relevant for $(g_i)_{\text{eff}}(t)$, but at the cost of an additional factor of t in front of the exponential, which may be important at intermediate values of t.

Alternatively to taking the derivative as in Eq. (B4), one may fit $S_i(t)$ using the linear function (B3) with parameters c_i and $(g_i)_{\text{eff}}$. In Fig. 19, we show numerical results for $S_i(t)$, along with such fits. In Fig. 20, we compare numerical results for the standard ratio (B1), the derivative of the summed ratio (B4), and the results for $(g_i)_{\text{eff}}$ from linear fits to $S_i(t)$ using Eq. (B3). For our data, the results from the summation method, especially for the derivative of the summed ratio, are seen to suffer from much larger statistical uncertainties than the standard ratio. This was also found in Ref. [80] and is not unexpected, because the relative statistical uncertainty in the difference of two similarly-sized observables (the discrete derivative used here) is much larger than the relative statistical uncertainty in the individual observables. Of course there are correlations which can improve the situation, and we did take these into account when calculating (B4), but because of the way that our lattice calculation was set up (data at successive values of t did not always have neighboring source locations), the correlations were not optimal.

It appears that the systematic errors of the results from the summation method at short t are similar in magnitude to the systematic errors of the results from the standard ratio method at the same t, but the deviations from (g_i)eff have the opposite sign. This shows that valuable information about systematic errors can be obtained by comparing both methods. For the present data, our process of extrapolating the results from the standard ratio to infinite t is superior because of the much smaller statistical uncertainty.

Similarly to the work done in Ref. [80], we also studied models for the three-point and two-point functions with

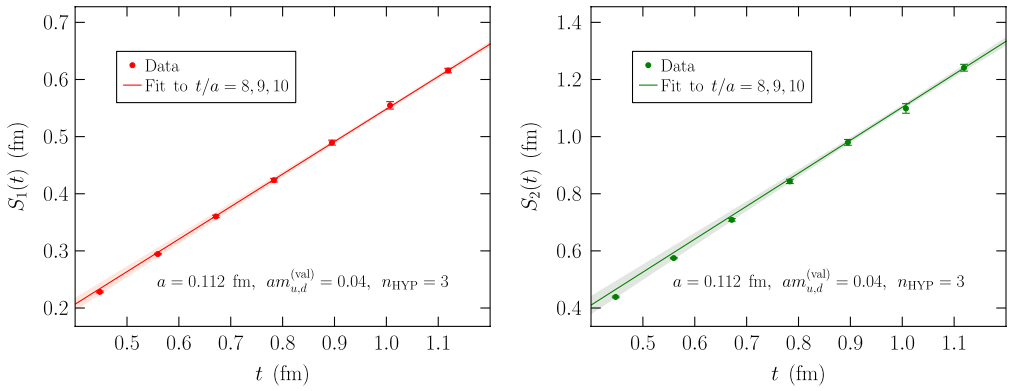

FIG. 19 (color online). Fits to the summed ratios $S_1(t)$ and $S_2(t)$, in the range $t/a = 8, 9, 10$. The data are for $a = 0.112$ fm, and a heavy-quark mass of $m_{u,d}^{(\text{val})} = 0.04$ (close to the physical strange-quark mass; the large mass was chosen here for the smaller statistical uncertainties) and $n_{\text{HYP}} = 3$.

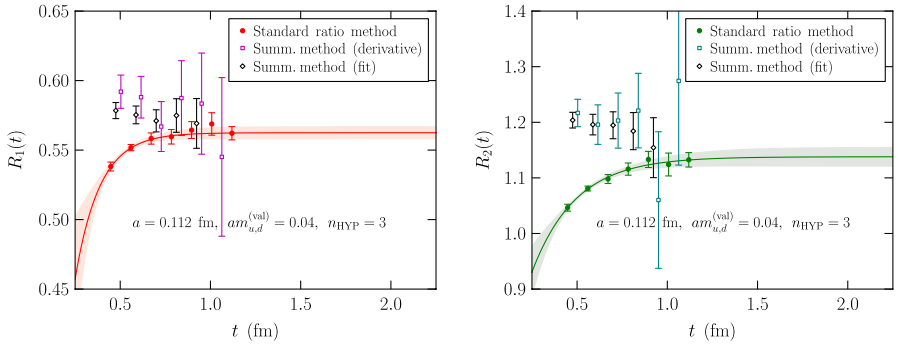

FIG. 20 (color online). Comparison of the standard ratio method and the summation method for R_1 and R_2 at $a = 0.112$ fm, for a heavy-quark mass of $am_{u,d}^{(\mathrm{val})} = 0.04$ (close to the physical strange-quark mass; the large mass was chosen here for the smaller statistical uncertainties) and $n_{\mathrm{HYP}} = 3$. Shown is the dependence on the source-sink separation t. The derivative of the summed ratio, Eq. (B4), is approximated using $R_i^{\mathrm{sum}} = [S_i(t) + S_i(t + a)]/a$ and plotted with square symbols at $t + \frac{1}{2}a$. The results for $(g_i)_{\mathrm{eff}}$ from linear fits to $S_i(t)$ using Eq. (B3) are plotted with diamond symbols. We performed fits in the range $t = t_{\mathrm{min}} \ldots 10a$, and the results are plotted at $t = t_{\mathrm{min}} + \frac{1}{4}a$. For the data from the standard ratio method (circles), the curves indicate the results of fits with the form $R_i(t) = (g_i)_{\mathrm{eff}} - A_i e^{-\delta_i t}$ with free parameters $(g_i)_{\mathrm{eff}}$, A_i, and δ_i see Sec. IV B.

excited states. We found that at intermediate values of t, the systematic uncertainties of (B1) and (B4) were strongly dependent on the assumptions made in the model. For some models, the standard ratio showed an adantage while for others the summation method showed an advantage, so that again we were not able to draw definitive conclusions.

Further methods for the calculation of hadron-to-hadron matrix elements are based on the generalized eigenvalue problem [80] and the "generalized pencil-of-function" [81]. These techniques use matrices of correlation functions with multiple interpolating fields to reduce the excited-state contamination at finite t. Because we only have data from one interpolating field for each hadron, we cannot test these methods here.

[1] J. Gasser and H. Leutwyler, Ann. Phys. (N.Y.) **158**, 142 (1984).
[2] M. A. Shifman and M. B. Voloshin, Sov. J. Nucl. Phys. **47**, 511 (1988).
[3] M. B. Wise, Phys. Rev. D **45**, R2188 (1992).
[4] G. Burdman and J. F. Donoghue, Phys. Lett. B **280**, 287 (1992).
[5] T.-M. Yan, H.-Y. Cheng, C.-Y. Cheung, G.-L. Lin, Y. C. Lin, and H.-L. Yu, Phys. Rev. D **46**, 1148 (1992); **55**, 5851 (E) (1997).
[6] P. L. Cho, Phys. Lett. B **285**, 145 (1992).
[7] P. L. Cho, Nucl. Phys. **B396**, 183 (1993); **B421**, 683(E) (1994).
[8] H.-Y. Cheng, C.-Y. Cheung, G.-L. Lin, Y. C. Lin, T.-M. Yan, and H.-L. Yu, Phys. Rev. D **49**, 5857 (1994); **55**, 5851 (E) (1997).
[9] B. Grinstein, E. E. Jenkins, A. V. Manohar, M. J. Savage, and M. B. Wise, Nucl. Phys. **B380**, 369 (1992).
[10] J. L. Goity, Phys. Rev. D **46**, 3929 (1992).
[11] C. G. Boyd and B. Grinstein, Nucl. Phys. **B442**, 205 (1995).
[12] A. S. Kronfeld and S. M. Ryan, Phys. Lett. B **543**, 59 (2002).
[13] T. Aaltonen *et al.* (CDF Collaboration), Phys. Rev. D **85**, 092011 (2012).
[14] G. M. de Divitiis, L. Del Debbio, M. Di Pierro, J. M. Flynn, C. Michael, and J. Peisa (UKQCD Collaboration), J. High Energy Phys. 10 (1998) 010.
[15] A. Abada, D. Bećirević, P. Boucaud, G. Herdoiza, J. P. Leroy, A. Le Yaouanc, and O. Pene, J. High Energy Phys. 02 (2004) 016.
[16] S. Negishi, H. Matsufuru, and T. Onogi, Prog. Theor. Phys. **117**, 275 (2007).
[17] H. Ohki, H. Matsufuru, and T. Onogi, Phys. Rev. D **77**, 094509 (2008).
[18] D. Bećirević, B. Blossier, E. Chang, and B. Haas, Phys. Lett. B **679**, 231 (2009).
[19] J. Bulava, M. A. Donnellan, and R. Sommer (ALPHA Collaboration), Proc. Sci., LATTICE2010 (2010) 303.
[20] W. Detmold, C.-J. D. Lin, and S. Meinel, Phys. Rev. D **84**, 094502 (2011).
[21] W. Detmold, C.-J. D. Lin, and S. Meinel, Phys. Rev. Lett. **108**, 172003 (2012).
[22] E. Eichten and B. R. Hill, Phys. Lett. B **240**, 193 (1990).
[23] M. Della Morte, S. Dürr, J. Heitger, H. Molke, J. Rolf, A. Shindler, and R. Sommer (ALPHA Collaboration), Phys. Lett. B **581**, 93 (2004); **612**, 313(E) (2005).

[24] D. B. Kaplan, Phys. Lett. B **288**, 342 (1992).
[25] Y. Shamir, Nucl. Phys. **B406**, 90 (1993).
[26] V. Furman and Y. Shamir, Nucl. Phys. **B439**, 54 (1995).
[27] Y. Aoki *et al.* (RBC/UKQCD Collaboration), Phys. Rev. D **83**, 074508 (2011).
[28] H. Georgi, Nucl. Phys. **B348**, 293 (1991).
[29] T. Aaltonen *et al.* (CDF Collaboration), Phys. Rev. Lett. **99**, 202001 (2007).
[30] H.-Y. Cheng, Phys. Lett. B **399**, 281 (1997).
[31] W. Detmold, K. Orginos, and M. J. Savage, Phys. Rev. D **76**, 114503 (2007).
[32] D. J. Antonio *et al.* (RBC/UKQCD Collaboration), Phys. Rev. D **75**, 114501 (2007).
[33] Y. Iwasaki, Report No. UTHEP-118, 1983.
[34] Y. Iwasaki and T. Yoshie, Phys. Lett. B **143**, 449 (1984).
[35] Y. Aoki *et al.*, Phys. Rev. D **69**, 074504 (2004).
[36] S. Meinel, Phys. Rev. D **82**, 114502 (2010).
[37] A. Hasenfratz and F. Knechtli, Phys. Rev. D **64**, 034504 (2001).
[38] G. P. Lepage, Nucl. Phys. B, Proc. Suppl. **26**, 45 (1992).
[39] T. Burch, C. Hagen, C. B. Lang, M. Limmer, and A. Schäfer, Phys. Rev. D **79**, 014504 (2009).
[40] C. Michael, A. Shindler, and M. Wagner (ETM Collaboration), J. High Energy Phys. 08 (2010) 009.
[41] B. Yoon, Y. C. Jang, C. Jung, and W. Lee, arXiv:1101.2248.
[42] B. Sheikholeslami and R. Wohlert, Nucl. Phys. **B259**, 572 (1985).
[43] D. Becirevic, E. Chang, and A. L. Yaouanc, arXiv:1203.0167.
[44] S. Fajfer and J. F. Kamenik, Phys. Rev. D **74**, 074023 (2006).
[45] P. Colangelo, F. De Fazio, and G. Nardulli, Phys. Lett. B **334**, 175 (1994).
[46] D. Bećirević and A. L. Yaouanc, J. High Energy Phys. 03 (1999) 021.
[47] Z. Guralnik, M. E. Luke, and A. V. Manohar, Nucl. Phys. **B390**, 474 (1993).
[48] P. Colangelo, G. Nardulli, A. Deandrea, N. Di Bartolomeo, R. Gatto, and F. Feruglio, Phys. Lett. B **339**, 151 (1994).
[49] V. M. Belyaev, V. M. Braun, A. Khodjamirian, and R. Rückl, Phys. Rev. D **51**, 6177 (1995).
[50] H. G. Dosch and S. Narison, Phys. Lett. B **368**, 163 (1996).
[51] P. Colangelo and F. De Fazio, Eur. Phys. J. C **4**, 503 (1998).
[52] D. Pirjol and T.-M. Yan, Phys. Rev. D **56**, 5483 (1997).
[53] S.-L. Zhu and Y.-B. Dai, Phys. Lett. B **429**, 72 (1998).
[54] P. L. Cho and H. Georgi, Phys. Lett. B **296**, 408 (1992); **300**, 410(E) (1993).
[55] M. C. Arnesen, B. Grinstein, I. Z. Rothstein, and I. W. Stewart, Phys. Rev. Lett. **95**, 071802 (2005).
[56] X.-Q. Li, F. Su, and Y.-D. Yang, Phys. Rev. D **83**, 054019 (2011).
[57] E. E. Jenkins, Phys. Lett. B **315**, 431 (1993).
[58] J. F. Amundson, C. G. Boyd, E. E. Jenkins, M. Luke, A. V. Manohar, J. L. Rosner, M. J. Savage, and M. B. Wise, Phys. Lett. B **296**, 415 (1992).
[59] I. W. Stewart, Nucl. Phys. **B529**, 62 (1998).
[60] A. Anastassov *et al.* (CLEO Collaboration), Phys. Rev. D **65**, 032003 (2002).
[61] M. A. Ivanov, J. G. Körner, V. E. Lyubovitskij, and A. G. Rusetsky, Phys. Rev. D **60**, 094002 (1999).
[62] H.-Y. Cheng, C.-Y. Cheung, G.-L. Lin, Y. C. Lin, T.-M. Yan, and H.-L. Yu, Phys. Rev. D **49**, 2490 (1994).
[63] K. Nakamura *et al.* (Particle Data Group), J. Phys. G **37**, 075021 (2010).
[64] S. Tawfiq, P. J. O'Donnell, and J. G. Körner, Phys. Rev. D **58**, 054010 (1998).
[65] C. Albertus, E. Hernandez, J. Nieves, and J. M. Verde-Velasco, Phys. Rev. D **72**, 094022 (2005).
[66] E. Hernandez and J. Nieves, Phys. Rev. D **84**, 057902 (2011).
[67] H.-Y. Cheng and C.-K. Chua, Phys. Rev. D **75**, 014006 (2007).
[68] C.-W. Hwang, Eur. Phys. J. C **50**, 793 (2007).
[69] C. Chen, X.-L. Chen, X. Liu, W.-Z. Deng, and S.-L. Zhu, Phys. Rev. D **75**, 094017 (2007).
[70] S. Chatrchyan *et al.* (CMS Collaboration), arXiv:1204.5955.
[71] L. Gibbons *et al.* (CLEO Collaboration), Phys. Rev. Lett. **77**, 810 (1996).
[72] P. Avery *et al.* (CLEO Collaboration), Phys. Rev. Lett. **75**, 4364 (1995).
[73] M. Lu, M. J. Savage, and J. Walden, Phys. Lett. B **369**, 337 (1996).
[74] T. Aaltonen *et al.* (CDF Collaboration), Phys. Rev. Lett. **107**, 102001 (2011).
[75] E. E. Jenkins and A. V. Manohar, *Proceedings of the Workshop on Effective Field Theories of the Standard Model, Dobogókő, Hungary, 1991*, edited by U.-G. Meissner (World Scientific, Singapore, 1992) (Report No. UCSD/PTH 91-30).
[76] E. E. Jenkins and A. V. Manohar, Phys. Lett. B **255**, 558 (1991).
[77] L. Maiani, G. Martinelli, M. L. Paciello, and B. Taglienti, Nucl. Phys. **B293**, 420 (1987).
[78] S. Güsken, U. Low, K. H. Mutter, R. Sommer, A. Patel, and K. Schilling, Phys. Lett. B **227**, 266 (1989).
[79] S. Capitani, B. Knippschild, M. Della Morte, and H. Wittig, Proc. Sci., LATTICE2010 (2010) 147.
[80] J. Bulava, M. Donnellan, and R. Sommer, J. High Energy Phys. 01 (2012) 140.
[81] C. Aubin and K. Orginos, AIP Conf. Proc. **1374**, 621 (2011).
[82] R. G. Edwards and B. Joó (SciDAC Collaboration, LHPC Collaboration, and UKQCD Collaboration), Nucl. Phys. B, Proc. Suppl. **140**, 832 (2005).